THESIS

REDUCTION OF METHANE EMISSIONS THROUGH IN-CYLINDER METHODS ON A LEAN-BURN FOUR-STROKE NATURAL GAS ENGINE

Submitted by

Justin Bayer

Department of Mechanical Engineering

In partial fulfillment of the requirements

For the Degree of Master of Science

Colorado State University

Fort Collins, Colorado

Summer 2023

Master's Committee:

Advisor: Daniel Olsen

Bret Windom
Kenneth Carlson

ABSTRACT

REDUCTION OF METHANE EMISSIONS THROUGH IN-CYLINDER METHODS ON A LEAN-BURN FOUR-STROKE NATURAL GAS ENGINE

The U.S. utilizes over 27 trillion cubic feet of natural gas per year for a wide range of uses, including heating and electricity production, according to the U.S. Energy Information Administration. Natural gas (NG) engines used to compress natural gas and generate electricity account for nearly one-quarter of the total methane emissions in the gathering and boosting sector. These methane emissions are referred to as fuel (methane) slip since they originate from the engine fuel supply and result from incomplete combustion. The primary mechanism leading to unburned methane is related to the engine crevice volume. The crevice volume is the region between the side of the piston and the cylinder wall. This region is particularly difficult for the flame to propagate into because the gap is generally smaller than the quench distance.

This research evaluates multiple in-cylinder methods to attempt to reduce the methane slip. One of the mitigation strategies is hydrogen blending with the engine's natural gas fuel supply as a means of methane reduction. Converge Computational Fluid Dynamics (CFD) and a Caterpillar G3516J model are implemented to analyze the effects of hydrogen blending. The G3516J engine is a lean-burn engine commonly used for gas compression in the US NG pipeline system. Converge CFD is a solver that couples combustion chemistry and adaptive mesh refinement to model combustion accurately. Simulations of combustion with NG-hydrogen blended fuel are performed

with constant fuel energy, achieved by adjusting boost pressure at a constant equivalence ratio. Combustion cycle simulations are performed at various hydrogen blending levels, and the methane emissions are evaluated at the end of the cycle and compared. In addition, the fuel mixtures' pressure is adjusted to reflect similar indicated power and a similar emission comparison is made. The second mitigation strategy that is explored is induced autoignition. This strategy involved advancing the engine's spark timing to hopefully increase the temperature and pressure in the cylinder to have the end-gas auto-ignite and thus burn more fuel that would otherwise become methane slip. This research also incorporates installing a G3516J engine at the Engines and Energies Conversion Laboratory.

Advancing the spark timing in the simulations did not show signs of end gas auto-ignition. Although this is the case, the advanced spark timing showed a decrease in unburned methane compared to the baseline. The spark timing with the lowest unburned CH4 percentage decreases from 3.00% to 2.26% by advancing the spark timing by ten crank angle degrees. The hydrogen blending also showed lower unburned CH4 percentages compared to the baseline. After adjusting the simulations to match indicated power output, the lowest results decreased the unburned percentage from 3.00% to 1.20%. NOx emissions were increased by 129% compared to the baseline in the most extreme simulation case. Leaning the fuel mixture lowered the NOx emissions to within 6% of the baseline while still lowering the unburned percentage from 3.00% to 2.67%.

TABLE OF CONTENTS

LIST OF TABLES

LIST OF FIGURES

CHAPTER 1- INTRODUCTION

1.1 Background

Over twenty-seven trillion cubic feet of natural gas is consumed a year by the U.S. for an extensive range of uses which include heating and electricity production, according to the Energy Information Administration [1]. Natural gas is comprised of many hydrocarbon molecules, the primary constituent being methane (CH_4). Methane is a stable molecule due to the carbon atoms' covalent bonds with the hydrogen atoms. Methane is considered a greenhouse gas and must be accounted for when analyzing engine emissions. According to the EPA, methane is 25 times more potent than a greenhouse gas, compared to CO2 over 100 years [2]. Methane's greenhouse effect, combined with new government mandates such as the "Good Neighbor" provision under the Clean Air Act, signifies that the methane emissions for stationary combustion engines, like Caterpillar's® G3516J engine, require further investigation as they account for nearly 24% of the total methane emissions that come from the gathering and boosting sector [3]. In 2023, the Department of Energy announced that $22.5 million would go towards projects that are focused on developing strategies such as the reduction of emissions in the industrial and manufacturing sector [4]. Lastly, methane emissions represent a wasteful use of resources, consequently inflating fuel costs. Natural gas combustion engines produce methane emissions that makeup 6% of makeup natural gas system emissions [3]. The fuel is injected into the engine, but due to inefficiencies part of the fuel does not combust and is expelled into the environment, leading to decreased engine efficiency and overall power losses.

1.2 Problem

Hydrocarbons, such as CH_4, are molecules made of hydrogen and carbon atoms. Due to their high energy densities and relative stability, hydrocarbons are utilized as fuel. Breaking the carbon-hydrogen bonds releases energy, in the form of heat, which can be used to power machinery, e.g., combustion engines. The prominent challenge with the combustion process is that the reactants (air and fuel) do not completely react, and residuals of the reactants are present after combustion. To best understand the underlying cause of methane emissions, it is important to discuss the basic principles of combustion. First, the reactants are deposited into each engine cylinder. Meanwhile, the piston starts its upward stroke which compresses the mixture increasing the pressure and temperature of the mixture. At a predetermined optimal point in the engine cycle, a sparkplug is used to ignite the mixture. The spark generated from the spark plug begins the combustion process, which is limited to the flame speed and adiabatic flame temperature of the fuel.

$$H_{reac} = H_{prod} = \sum N_i[\bar{h}^o_{f,i} + \bar{c}^o_{p,i}\,(T_{ad} - 298)] \qquad \text{(Eqn. 1)}$$

Equation 1 helps better understand the temperature of the adiabatic flame, assuming constant pressure [5]. The H_{reac} is the enthalpy of the reactants, N_i is the number of moles, $h^o_{f,i}$ is the enthalpy of formation, $c^o_{p,i}$ is specific heat, and T_{ad} is the adiabatic temperature in Kelvin.

$$S_L = (2\alpha)/\delta \qquad \text{(Eqn. 2)}$$

Equation 2 obtains laminar flame speed, S_L, by utilizing thermal diffusivity, α, and laminar flame thickness, δ [5]. These two equations help describe how combustion occurs

in an engine. Equation 1 is used to find the temperature at which combustion will occur while Equation 2 helps describe how fast the combustion flame will travel. Another significant contributor to combustion is engine geometry. Figure 1 shows the cross-section of a cylinder and associated piston, of a Caterpillar® G3516J engine. Rings are integrated into the piston design which allows the piston skirt and the cylinder sidewall to form a tight seal, even as the piston moves. The issue with these piston rings is that they form a crevice volume. The methane that enters this volume tends to avoid combustion because the nearby cylinder walls are relatively cold compared to the combustion flame, therefore creating a significant loss of heat when the flame is near. This heat transfer occurs between the flame and the cylinder wall which causes the flame to quench and leaves unburned fuel in the crevice volume. In a study by G. Konig et. al, it was found that as much as 6.1% of the total mass in the cylinder could be found in the top land crevice at a specified point during an engine cycle [6].

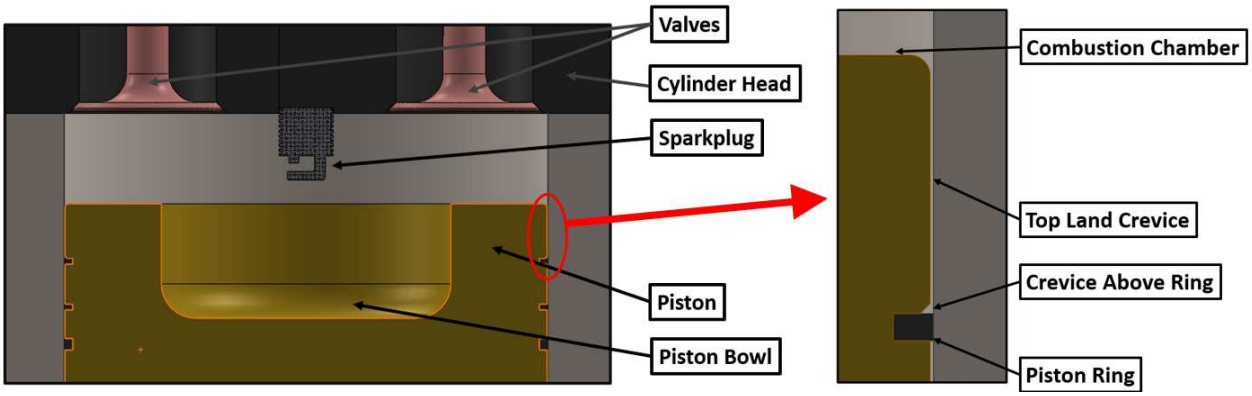

Figure 1. Cross section of an engine cylinder, piston, and piston rings. The red circle highlights the crevice volume.

1.3 Previous Research

Methane emission reduction techniques in lean-burn 4-stroke natural gas engines, such as the G3516J, is a relatively unexplored field of research. The remainder of this section will discuss previous research conducted in the area of methane reduction and will give an idea of the strategies that are either in use today or continue to be studied.

1.3.1 Catalyst

One hydrocarbon emission reduction strategy is the utilization of a catalytic converter. Catalysts oxidize the fuel in the exhaust, converting unburned hydrocarbons into less environmentally harmful molecules like water and CO_2. For CH_4 to be oxidized, the elements palladium, rhodium, or platinum are commonly used in catalytic converters. A study by Kevin Smith [7] found a potential reduction of 50-60% methane through this type of system when used on a stoichiometric-burn engine. Because lean burn engines like the G3516J have cooler exhaust temperatures compared to a rich burn engine, the effectiveness of a three-way catalyst on ethane emissions is much less. Another downside is the production of water in the exhaust products. The water can be harmful to rare earth metals and decrease the effectiveness of reducing CH_4 emissions. Figure 2 shows the effects of water in a catalytic converter. The gold line shows that without water present, CH_4 conversion is nearing 100%. This efficiency drops to about 60% when water is present [8].

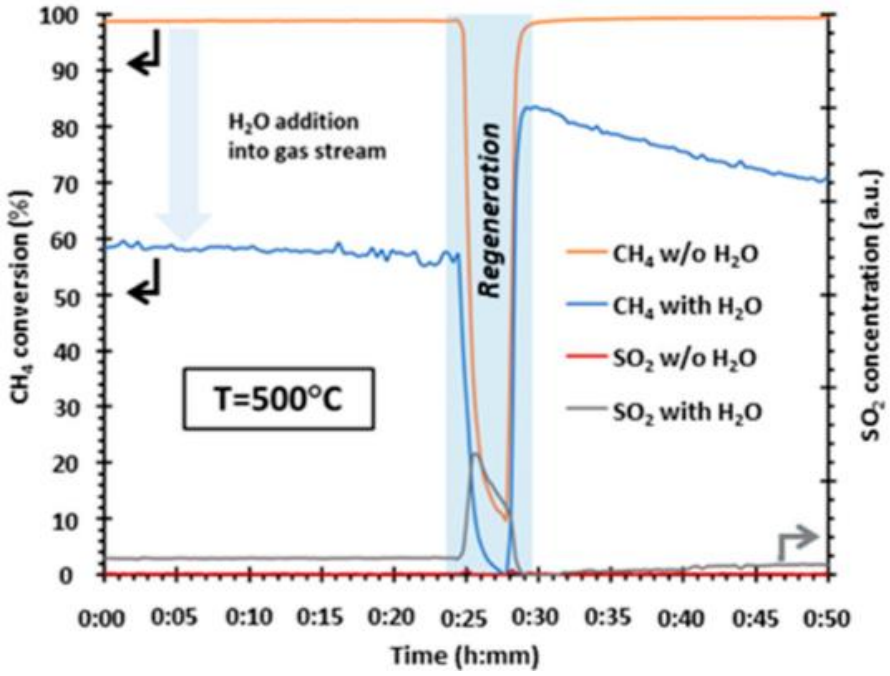

Figure 2. This graph highlights the change that water in the catalyst can have (~40% reduction in CH4 conversion) [8].

1.3.2 Reverse Flow Reactors

A second method used in reducing methane emissions is through a process of implementing reverse flow reactors. These systems work by using a reactor (type of catalyst) as a form of after-combustion treatment for engine emissions, specifically methane. The reactors alter (reverse) the engine emissions gas flow back and forth between four valves, which leads to an increase in the temperature of the unburned methane gas leading into the reactor. The temperature increase of the methane helps increase the oxidation efficiency in the reactor, consequently lowering CH_4 emissions. A figure of the four valves used as well as temperature plots are shown below in Figure 3. A study by Salomon, S, et. al [9] found that this process can lead to a reduction of methane at a rate of around 19%.

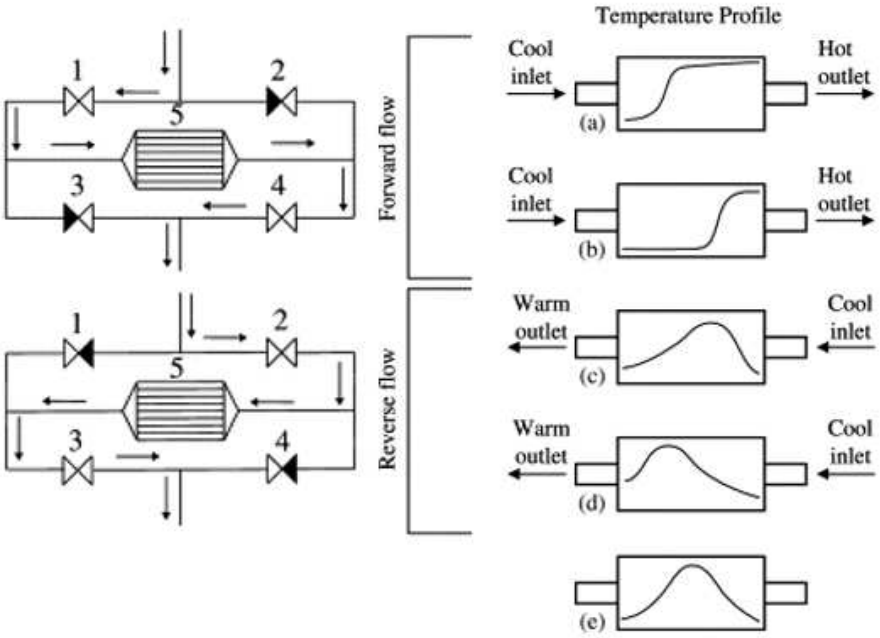

Figure 3. This figure shows valve orientations used in a reverse flow reactor and temperature profiles of exhaust flow [9].

1.3.3 Synthesis Reformate/ Fuel Additives

The utilization of synthesis reformate is an additional method used in reducing CH_4 emissions. This process involves mixing supplementary fuels (typically made of hydrogen and carbon monoxide) with natural gas before entering the combustion chamber. This new gas mixture has an increased reactivity, compared to natural gas alone, meaning that the flame speed and adiabatic flame temperature will be increased (Equations 1 and 2). This higher flame speed increases the reach of the flame into areas of the cylinder previously uninhabited, burns more fuel, and creates lower CH_4 emissions by increasing combustion efficiency. The higher adiabatic flame temperature also contributes to lower CH_4 emissions due to its increased resistance to quenching near the cylinder walls. In a study performed on a stoichiometric-burn engine, Nadaleti, W. C., & Przybyla, G found

that there was a significant decrease in hydrocarbon emissions when using syngas that contained varying amounts of hydrogen compared to methane as a base fuel [10]. This can be seen in Figure 4 which highlights their findings on hydrocarbon emissions. The graphs in the figure also show the differences in the syngas mixtures.

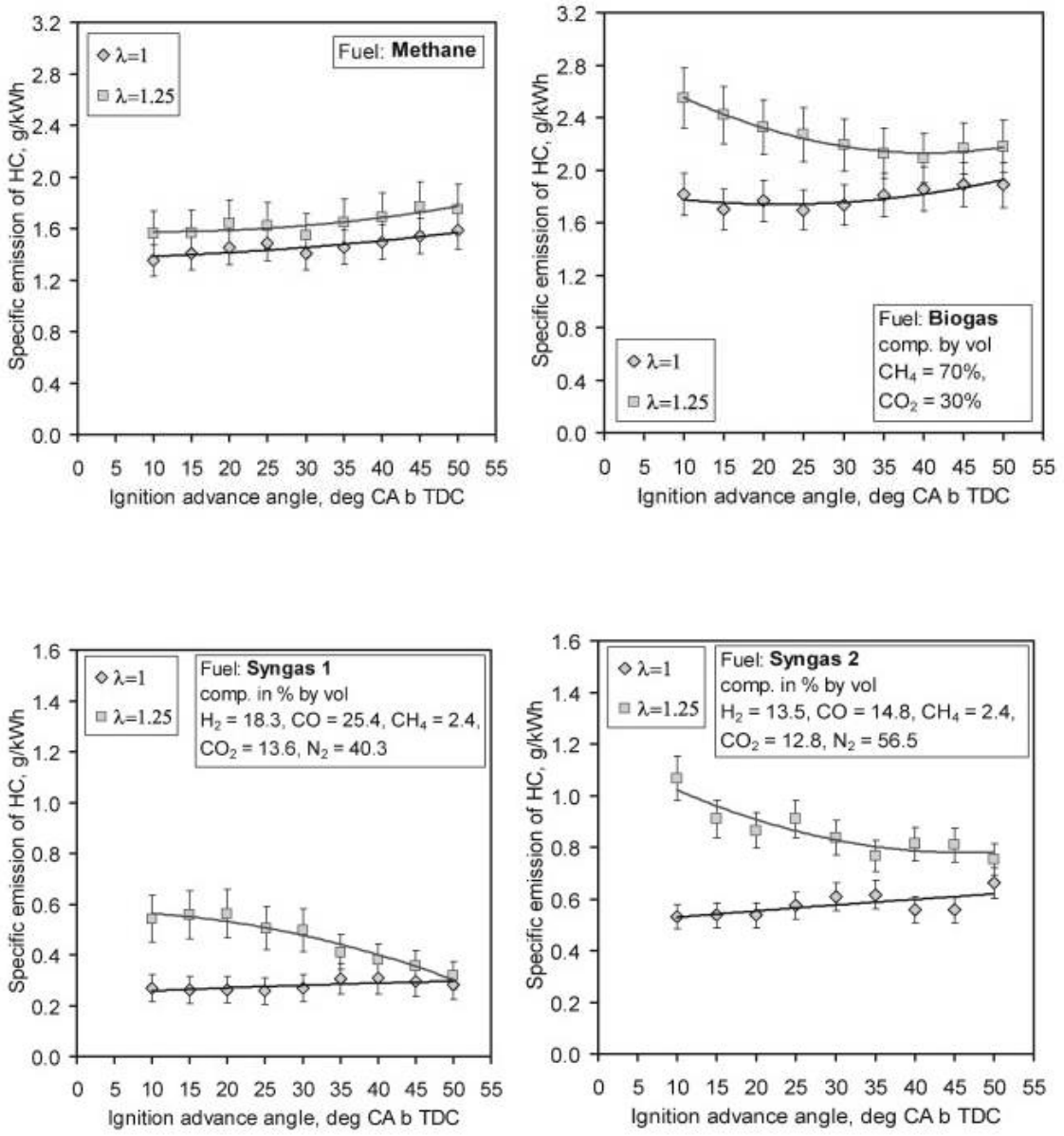

Figure 4. Specific emissions of hydrocarbons vs. ignition advance angle for various fuel blends [10].

Another alteration to fuel in an attempt to lower methane emissions is blending in a more reactive fuel, such as hydrogen. This is similar to syngas reformate but typically uses a purer form of more reactive fuel like hydrogen. This purer reactive fuel is then blended with natural gas. As illustrated in a study by Thomas Wallner et. al. [11], methane emissions were found to be lower as hydrogen was blended with methane. This can be seen in Figure 5 which depicts the methane emissions for different hydrogen blends vs spark timing. It was surmised in this study that the most probable cause for the emissions reduction was hydrogens' shorter quenching distance, effectively letting the flame reach closer to the engine wall. This study does not address the creation of NOx emissions as a tradeoff for burning more CH4 and having H2 substitution. The emissions would most likely change if NOx emissions matched the gas mixture with no H2 substitution.

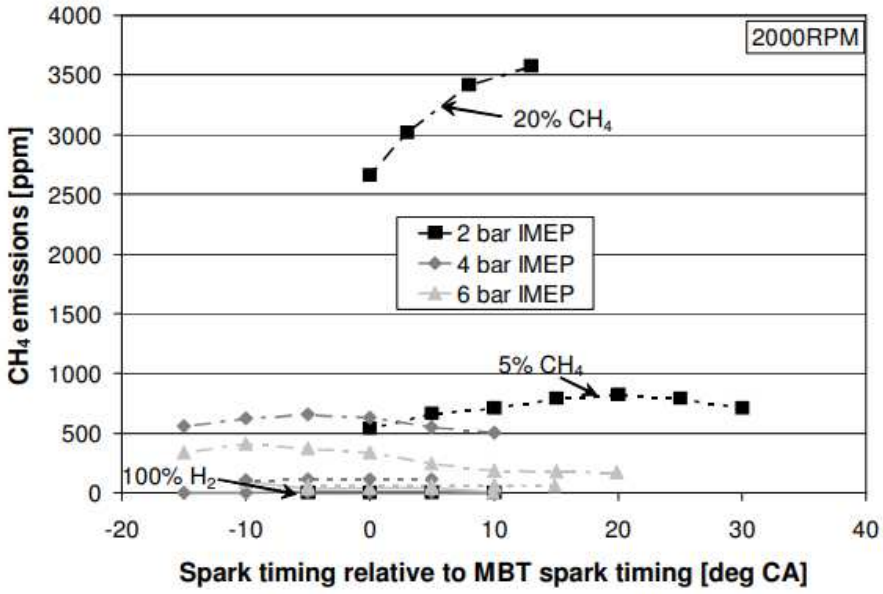

Figure 5. CH4 emissions vs Spark timing for different blends of methane and hydrogen [11].

1.3.4 End Gas Auto-Ignition (EGAI)

As a final method for discussion, CH_4 emissions can be reduced by inducing end gas auto-ignition. As stated previously, the combustion process is initialized by the spark plug. The generated spark ionizes the surrounding gas which creates a flame kernel that grows into a full flame. Most often, a slow flame speed, combined with wall quenching, leaves areas like the crevice volume (figure 1) filled with unburned fuel. End gas auto-ignition is one strategy that can be used to mitigate this issue. One way to induce end gas auto-ignition is to advance the spark timing. Advancing the spark timing allows more time for the flame to propagate through the cylinder, as a result creating an increase in the pressure and temperature of the fuel and air. If the pressure and temperature are increased to a high enough level, it can cause the fuel and air mixture that is in front of the combustion flame to ignite, effectively burning more fuel and lowering emissions (Figure 6) [12]. This type of emission control has been investigated on Colorado State University's Cooperative Fuel research engine. There it was found that EGAI can have up to 20% reduction in CH_4 emissions in stoichiometric natural gas engines [13].

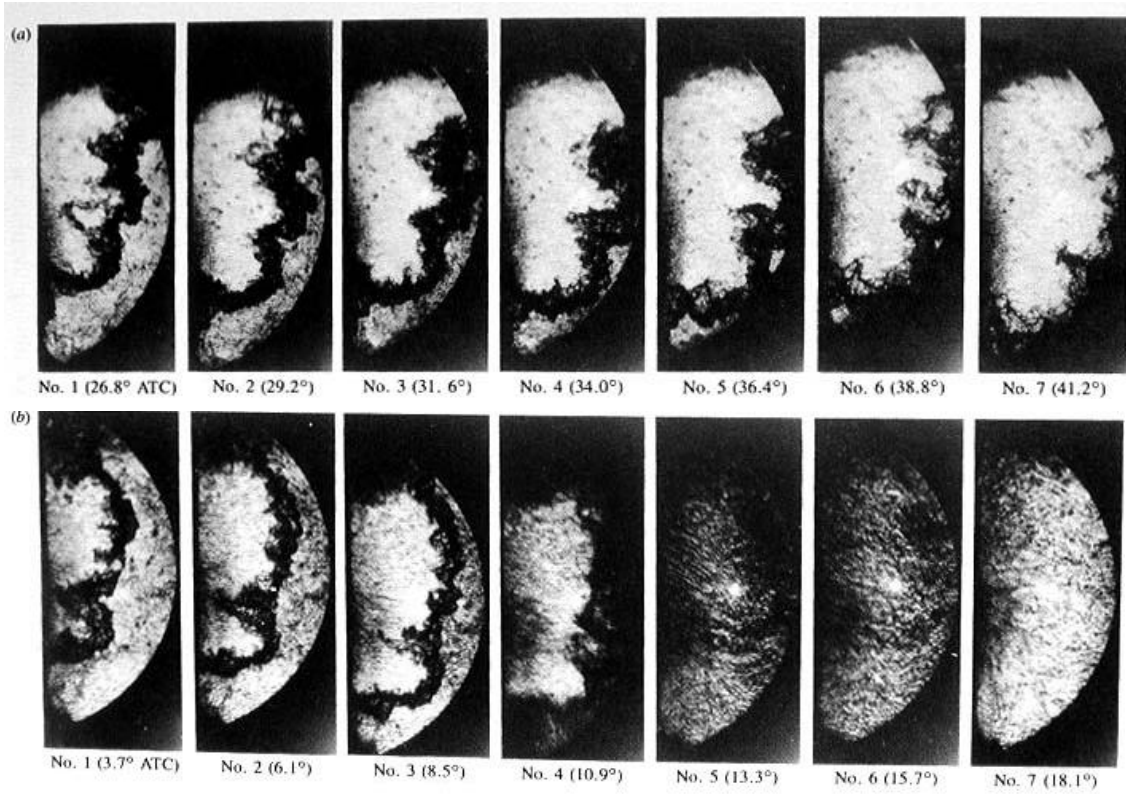

Figure 6. The above photos show what EGAI looks like inside a combustion chamber. A shows flame propagation without EGAI and B shows combustion with EGAI [12].

An alternative to inducing EGAI by advancing spark timing is by mixing more reactive fuels with natural gas. This can also induce EGAI by lowering the pressure and temperature limits that restrict the end gas from auto-igniting. Soylu, S. et.al. created a combustion model that mixed propane with natural gas. This model showed changes in the flammability of the fuel/air mixture that made the reactants more prone to end gas auto-ignition [14]. Figure 7 depicts two graphs from this study and shows the pressure inside the cylinder vs the crank angle. The first graph shows how different amounts of propane affect the pressure inside an engine while holding the spark timing constant. The second graph shows the pressure differences based on advancing spark timing. From

this figure, it can be seen that substituting propane slightly increases and advances the peak pressures in the cylinder as well as when knock occurred.

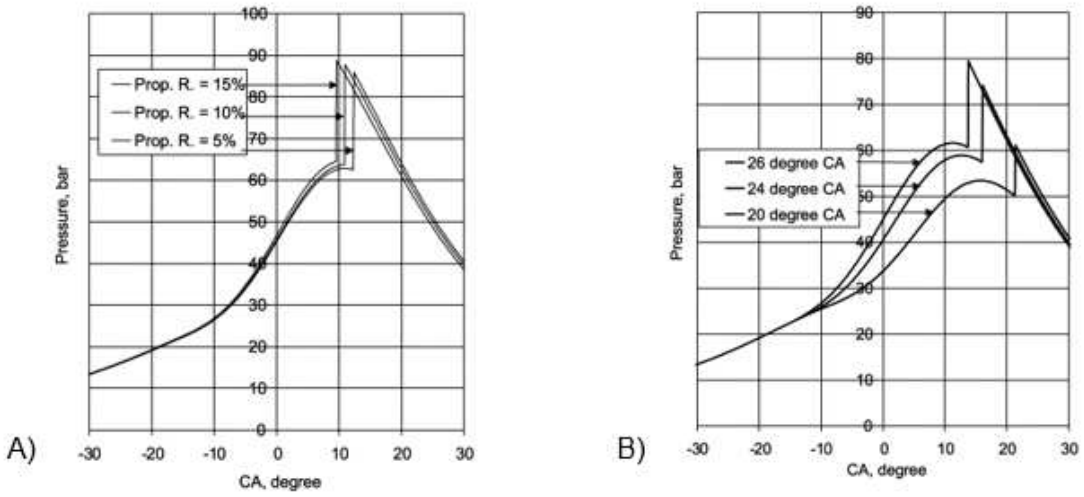

Figure 7. A) Pressure vs. Crank Angle with varying Propane Percentages. B) Pressure vs. Crank angle with varying spark timing [14].

Utilizing EGAI can be useful; however, there are potential drawbacks. The largest being engine knock. Knock occurs when the combustion from the end gas auto-ignition sends out a pressure wave, colliding with the pressure wave created from the initial spark-ignited combustion. The pressure waves collide causing an audible pressure spike. If the knock is too severe, the engine can be damaged. Figure 8 shows what a typical pressure curve vs crank angle (CA) looks like compared to one with a slight/intense knock. The spikes of pressure can also lead to increases in temperature and thus can damage internal engine components.

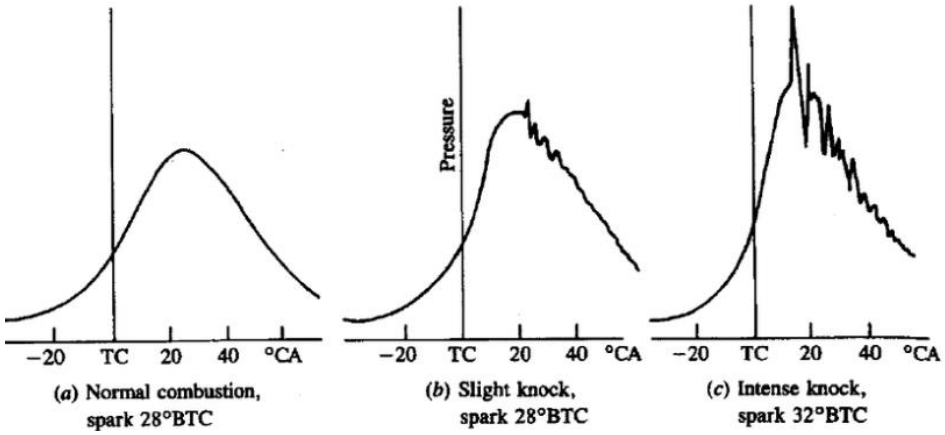

Figure 8. Pressure vs CA for normal combustion, slight knock, and intense knock. [12]

1.4 Summary

The emissions from current natural gas combustion engines operating in large stationary gas transportation units emit substantial amounts of methane into the environment. Methane is the main constituent of natural gas and has a greater global warming potential impact than carbon dioxide. A significant amount of research has been conducted to reduce engine-out methane emissions, but unfortunately, critical gaps remain. This research involves evaluating numerous in-cylinder methods for improving combustion engines to reduce engine-out methane emissions. Chapter 2 will focus primarily on the methods used in exploring these emission reduction strategies, including the use of computational fluid dynamics (CFD) software to model a single cylinder of Caterpillar's® G3516J engine. Chapter 3 will discuss the results that came from a baseline CFD model. The chapter also includes the simulation findings for reducing the size of the crevice volume and, separately, advancing spark timing to induce EGAI. Finally, emissions result from blending hydrogen with natural gas at various substitution

percentages. The results also include an analysis of the effects fuel blending has on nitrous oxide (NO_x) emissions, and a potential strategy to mitigate them. Chapter 4 will contain the installation of the G3516J engine that is modeled in the CFD software at Colorado State University. It will also include design considerations, as well as the removal of a Cummins 50-liter engine to make space for the G3516J. Chapter 5 contains the conclusions from this research as well as the next steps to carry this project into the future.

CHAPTER 2- METHODS AND MATERIALS

2.1.0 CFD Modeling Methods

To initiate the research, the first step is to create a baseline model for the Caterpillar G3516J engine. This modeling is done in Converge Computational Fluid Dynamics (CFD). Converge CFD pairs combustion chemistry, thermodynamics, and adaptive mesh refinement to accurately model combustion [15]. These models reduce costs associated with carrying out experiments and help avoid potential damage to physical equipment by predicting how an engine will behave. This software takes numerous inputs from known engine data and runs simulations to provide output parameters such as pressure, temperature, exhaust gas composition, and indicated engine power.

Converge CFD simulations take substantial computational time and computing power. Specifically, this research utilized a supercomputer with 128 cores on each of its 5 nodes. Each iteration of the full-cycle combustion simulation can take up to 5 days to complete. This means that strategies to reduce computational time while still making an accurate model are essential. The first of these strategies is modeling and testing only one cylinder. The results from the single cylinder can be multiplied to reflect the entire engine, while reducing the computational time by 16 based on a 16-cylinder engine. This individual cylinder includes sections of the head, engine block, intake and exhaust manifolds, a spark plug, and four valves. The single cylinder modeled for this research is shown in Figure 9. Figure 10 is a top-down view of the cylinder with the intake and exhaust manifolds removed. Figure 11 also shows a side view of the spark plug, including the center electrode, ground electrode, and spark plug gap.

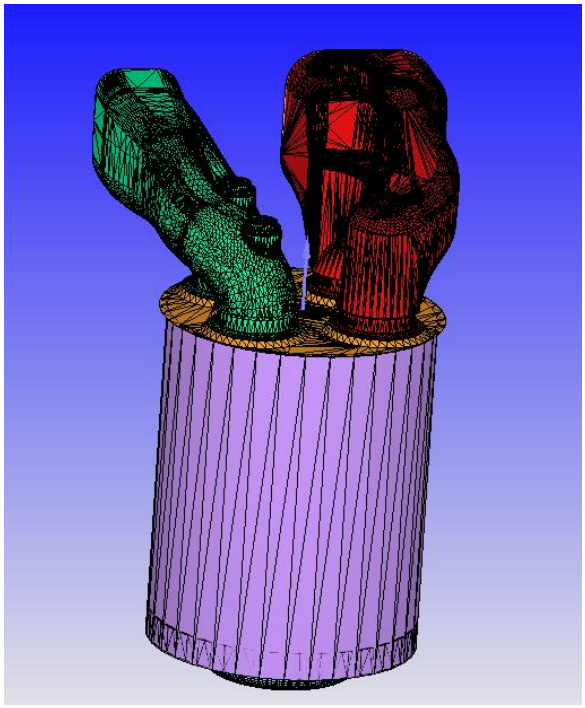

Figure 9. Converge rendering single-cylinder model. The red portion is the intake manifold, and the green portion is the exhaust manifold.

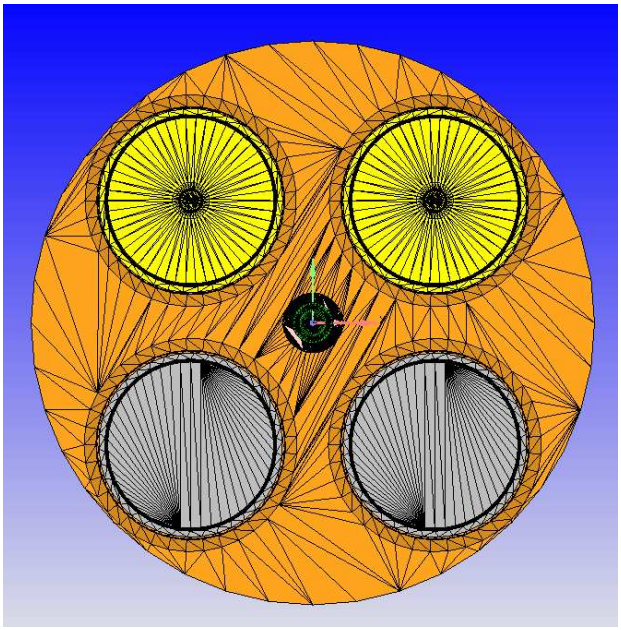

Figure 10. Top-down view of the model with the intake and exhaust manifolds removed to show the valves. The grey circles are the intake valves, and the gold circles are the exhaust valves. The dark center circle is the spark plug.

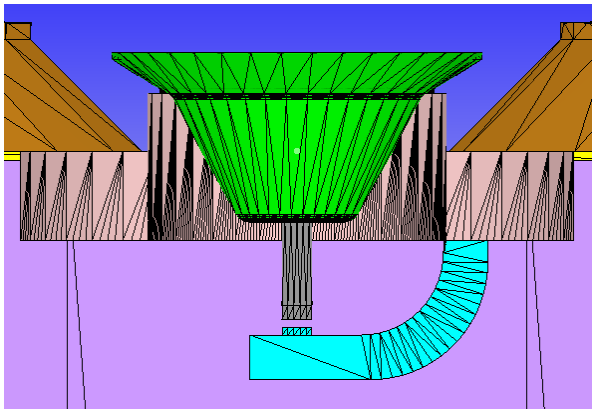

Figure 11. Side view of the spark plug that is modeled. The center electrode is the grey portion in the center of the figure and the ground electrode is the turquoise portion.

An additional strategy to reduce computational time is via mapping files. In Converge CFD, mapping files can be used to start simulations where others concluded. This mapping technology allows for multiple simulations to run with changes in input variables while negating the need to run full simulations. For example, in the case of advancing spark timing to induce EGAI, the intake portion of the engine cycle is run, and a mapping file is created before the spark timing occurs. This mapping file can then be used in multiple simulation cases with varying spark times, negating the need to run intake portions for every simulation. Reusing mapping files for multiple simulations isn't always a viable option. For example, simulations that have different gas mixtures need to be re-run to get the correct fuel into the cylinder. This is because the intake portion of the simulation occurs before a mapping file is created.

Furthermore, mapping files can reduce computational time by allowing for the negation of unnecessary engine geometries. After running the intake portion of the simulation, the intake valves are closed while the exhaust valves remain unopened. This means that modeling anything in between these two valve events negates the

requirement to model the intake or exhaust manifolds, ultimately saving computational time. Figure 12 shows a visual of the distinct simulation sections that are used in this research, including intake, compression/combustion, and exhaust. In the middle portion of the figure (compression/combustion), it is evident that no intake or exhaust manifold modeling occurred.

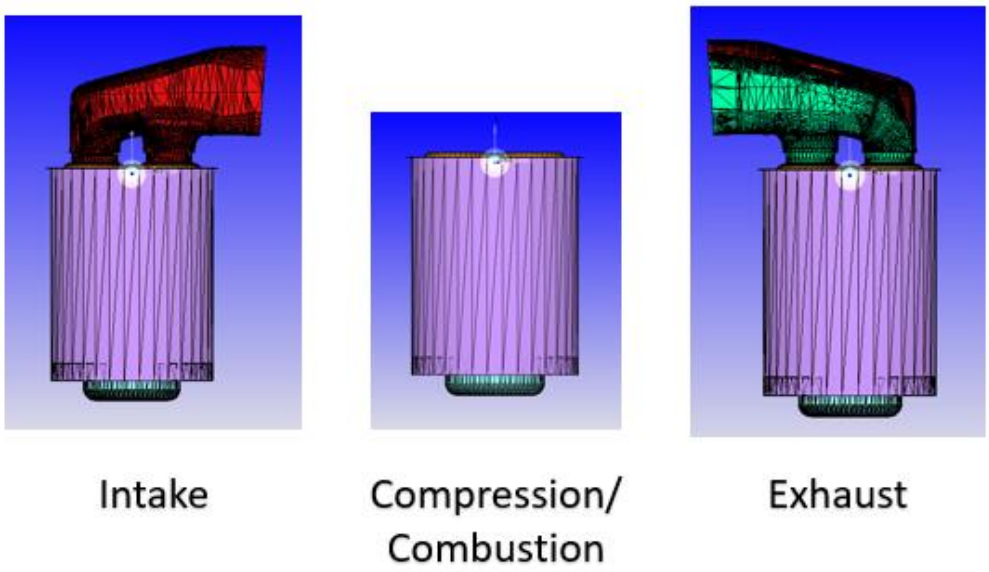

Figure 12. Three different model sections are used to divide Converge CFD simulations.

2.2.0 Mechanisms

Converge CFD utilizes combustion chemistry to accurately simulate engine combustion [15]. The combustion chemistry describes the chemical reaction between the fuel and air in the engine. The basic global reaction (unbalanced) that occurs in lean natural gas combustion is stated in Equation 3.

$$CH_4 + C_2H_6 + C_3H_8 + O_2 + N_2 => CO_2 + H_2O + N_2 + O_2 \qquad \text{(Eqn. 3)}$$

Equation 3 assumes that the three major species in natural gas fuel are methane, ethane, and propane as they are typically the three highest in concentration. This global

equation lacks significant insight as to how the actual combustion reaction takes place. Elementary reactions are sub-reactions that have the overall goal of describing the global reaction but with numerous steps involved. Reaction mechanisms are developed using elementary reaction combinations (mechanisms) to describe combustion. Figure 13 shows a small section of the elementary reactions from the GRI 3.0 Mechanism [16]. These mechanisms are inputted into Converge CFD and analyzed to get combustion data. Different mechanisms contain vastly different elementary reactions. These differences can drastically change how combustion is described in simulations, emphasizing the importance of choosing the best mechanism for the given engine parameters.

```
O+H2<=>H+OH
O+HO2<=>OH+O2
O+H2O2<=>OH+HO2
O+CH<=>H+CO
O+CH2<=>H+HCO
O+CH2(S)<=>H2+CO
O+CH2(S)<=>H+HCO
O+CH3<=>H+CH2O
O+CH4<=>OH+CH3
```

Figure 13. Sample of elementary reactions in the GRI 3.0 mechanism [16].

In this research, three different mechanisms were assessed for their validity to predict combustion. These included the San Diego Mechanism, the GRI 3.0 Mechanism, and the Aries 82 Mechanism [16-18]. An initial study was done in Converge CFD to compare these different mechanisms for ignition delay and flame speed over a range of pressures, temperatures, and equivalence ratios. The equivalence ratio (ER) relates the actual air-fuel ratio to a stochiometric air-fuel ratio, dependent on fuel composition. The equivalence ratio is given by Equation 4.

$$ER = \frac{(A/F)_{stoichiometric}}{(A/F)} \quad \text{(Eqn. 4)}$$

A is the air mass and F is the fuel mass. The air-to-fuel ratio in the numerator is the stoichiometric ratio, which indicates the exact amount of air is used to completely react with all of the fuel without having any excess air. The air-to-fuel ratio in the denominator is the actual air-to-fuel ratio that is present in the engine gas mixture. Because the engine model in this research is a lean burn engine, the actual air-to-fuel ratio is larger than the stoichiometric air-fuel ratio.

Ignition delay can provide insight surrounding the reactivity of the fuel, thus allowing for auto-ignition predictions. For example, if physical engine data shows signs of EGAI and the simulation is not, using a mechanism with a lower ignition delay may better represent the simulation's combustion. The flame speed can also offer insight into whether or not the combustion reaction is being accurately modeled. For example, CA 50 can be used to compare how combustion is occurring in an engine. CA 50 is the crank angle where 50 percent of the energy from the combustion reaction is released. If the simulation CA 50 occurs much later than what is expected from the physical engine data, a mechanism with a faster flame speed could help mitigate this issue and advance the CA 50 to adequately match the data.

Ignition delay is calculated using a 0-D simulation, while the laminar flame speed is evaluated using a 1-D simulation. These simulations do not consider engine geometry but rather compare how the fuel and air will react with a given equivalence ratio, temperature, and pressure. Figure 14 shows the laminar flame speed vs. temperature for the three mechanisms. To compare the different mechanisms, the equivalence ratio and pressure were held constant. Figure 15 shows the ignition delay at various equivalence

ratios for the mechanisms. The three mechanisms evaluated in this research are assessed to determine the best representation of the given engine data.

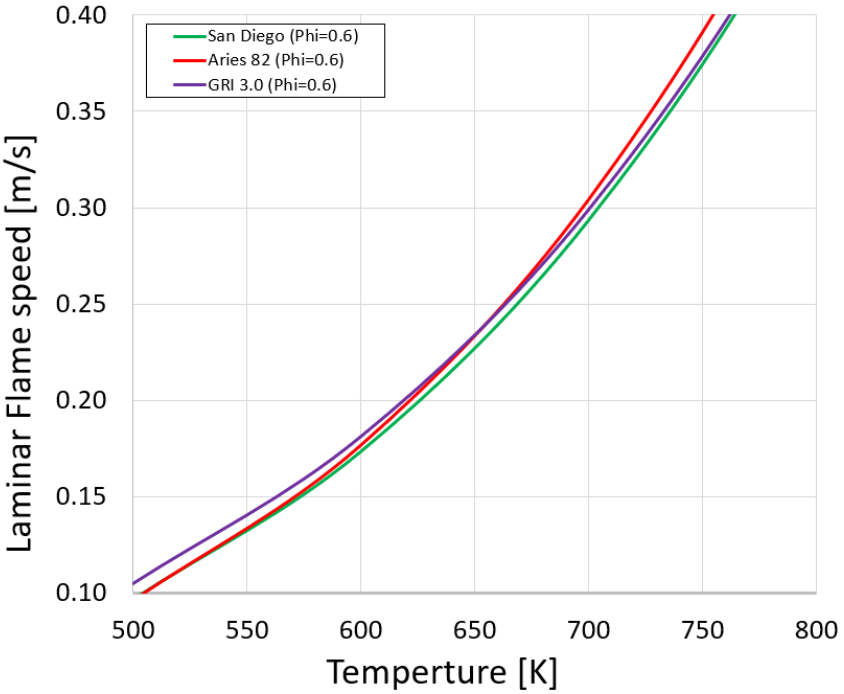

Figure 14. Laminar flame speed vs. temperature for different mechanisms.

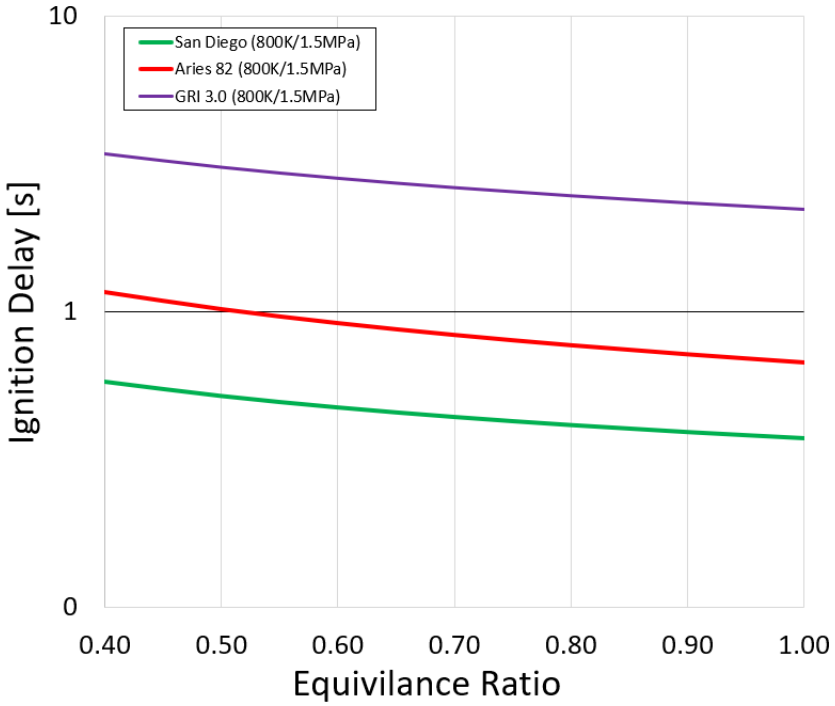

Figure 15. Ignition delay vs. Equivalence Ratio for different mechanisms.

2.3.0 Baseline Simulation

When modeling engines, it is critical to get an accurate baseline, allowing for a starting point for subsequent simulations under varied conditions. The accuracy of the model is assessed through the comparison of percent error for the trapped fuel mass per cylinder per cycle, equivalence ratio, brake work/power, and in-cylinder pressure (both peak pressure and location of peak pressure). Trapped mass is the amount of mass retained inside the cylinder after the intake valves are closed, including both fuel and air. All of these parameters are compared to known engine values for the G3516J.

2.3.1 Mesh

One of the initial steps to accurate engine modeling is adjusting the mesh of the simulation. Because Converge CFD cannot solve every single point in the engine, a mesh is used to choose specific points, which are calculated for parameters such as pressure and temperature throughout the simulation. This is called the base mesh. The base mesh needs to be fine enough to accurately depict all of the necessary areas, while also being coarse enough to let the simulation run in a reasonable amount of time. Figure 16 shows what the base mesh looked like inside the simulation.

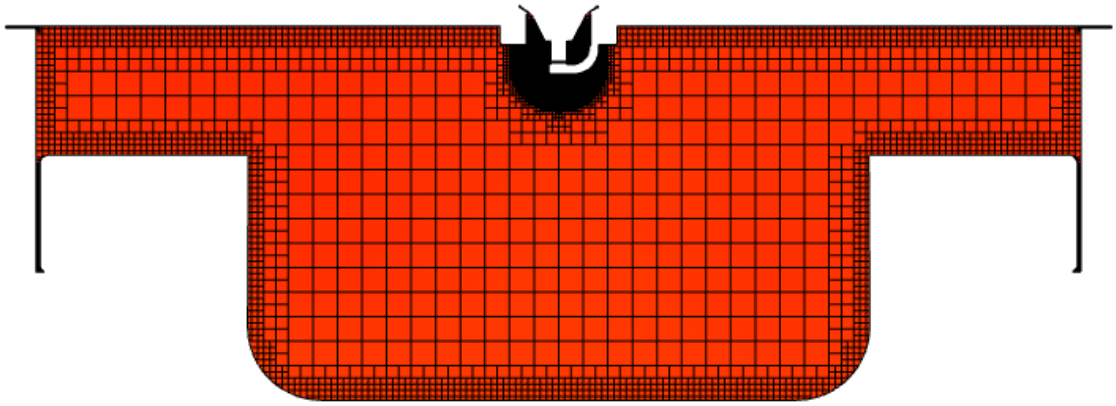

Figure 16. Cross section of combustion chamber highlighting the base mesh.

In addition to the base mesh, there are two additional mesh adjustments implemented to ensure accuracy. The first is an adaptive mesh refinement, which decreases the size of the mesh and makes it more accurate in specified areas based on the given parameters. The adaptive mesh refinement utilized in these simulations is engaged when large changes in velocity or temperature occur. The mesh becomes finer to accurately describe what is occurring in the simulation. For example, when the

combustion flame propagates, the temperature rises drastically. Figure 17 depicts how the mesh becomes more refined in this area. This figure shows a cross-section of the combustion chamber and depicts the mass fraction of CH4 inside the engine cylinder. The blue areas feature the lowest mass fraction of CH4 because combustion has already occurred in these areas, turning the fuel into exhaust products. The red area has the highest concentrations of CH4 due to its location in front of the combustion flame. The combustion flame is occurring where there are color gradients in between the red and blue areas. It can be seen from these pictures that the mesh is more refined in these areas of rapidly changing temperature.

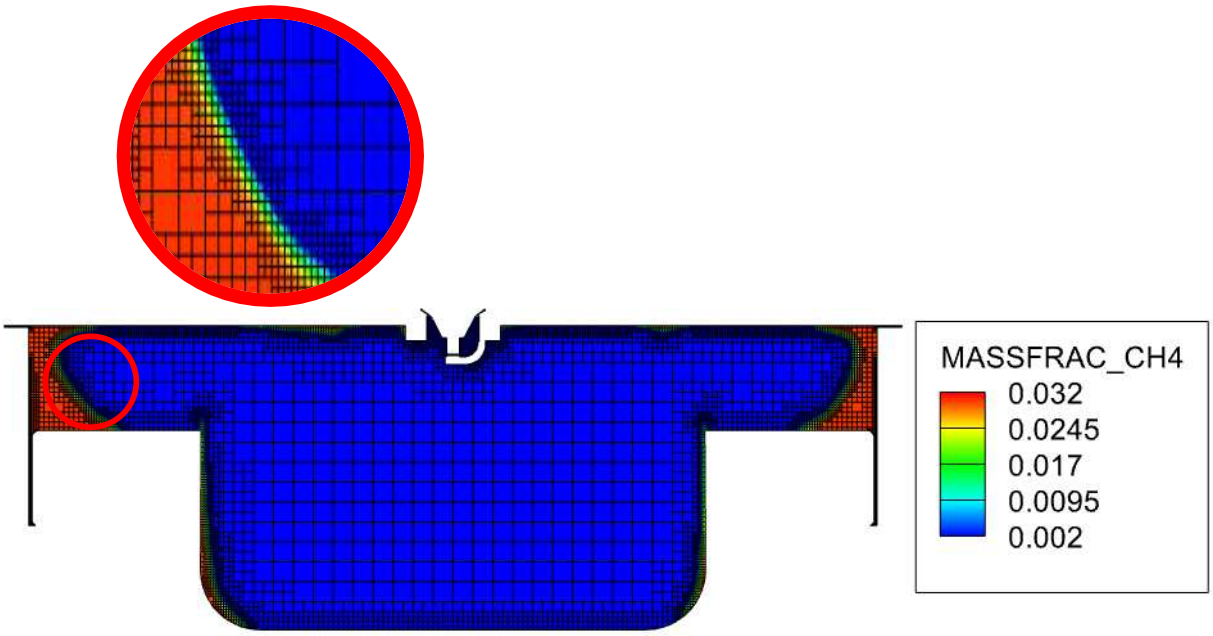

Figure 17. Cross section of combustion chamber highlighting the temperature-dependent adaptive mesh refinement.

The final type of mesh adjustment employed in the modeling is a fixed embedding mesh, which decreases the mesh size for specific areas. For example, in Figures 16 and 17, there is a finer mesh near the cylinder walls for increased accuracy. This is useful

when modeling emissions because a significant number of emissions occur near the walls as a result of flame quenching. Another example of fixed embedding is near the spark plug. After inducing a spark, a combustion flame kernel is created. It is relatively small and needs a fine mesh to accurately describe how this kernel transitions into a combustion flame. Figure 18 shows the areas near the spark plug that have fixed embedding mesh. The highlighted circle is where the kernel occurs and where the mesh is refined.

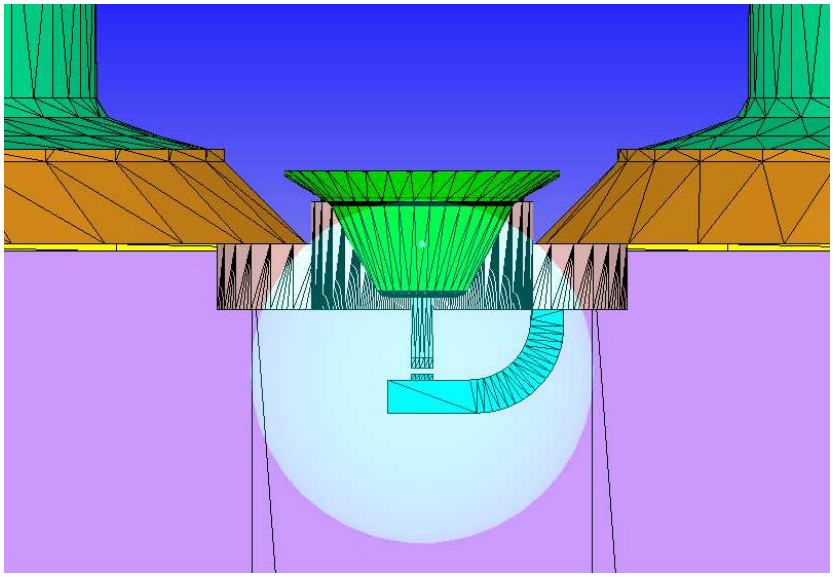

Figure 18. Simulation geometry showing where the fixed embedding mesh near the spark plug occurs.

2.3.2 Intake

After the mesh strategies are implemented, it is necessary to match the intake portion of the engine cycle to tune the baseline. This process required several parameters to be matched. The first parameter is the in-cylinder pressure. From previous G3516J engine data, the starting cylinder pressure is given and entered into the simulation in the form of a boundary condition. Figure 19 illustrates several

examples of the completed cycles set to match the initial pressure given by the data. Because the simulation is an iterative process that is constantly trying to converge to the correct value, it is apparent that the simulation data goes slightly above and slightly below the engine data at certain points, though it eventually converges to values similar to the engine pressure data.

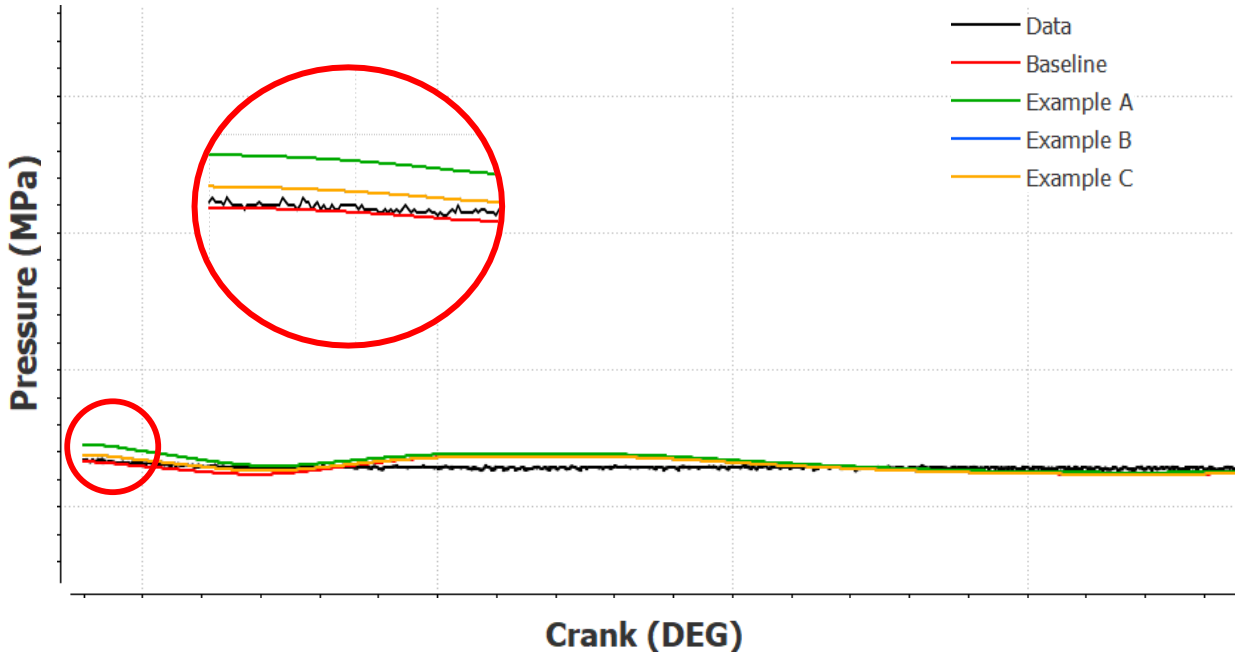

Figure 19. Pressure vs. crank angle emphasizes the iterations taken to match the initial in-cylinder pressure.

Some input parameters such as trapped fuel mass are not specifically outlined in the data and therefore need to be calculated. To begin this calculation, the molecular weight of the natural gas is calculated and combined with pressure, temperature, and volumetric flow rate data to find the fuel mass flow rate. The mass flow rate is then used to determine the mass of fuel per cylinder per cycle. This calculation is done using Equation 5.

$$Mass\ of\ fuel\ per\ cylinder\ per\ cycle\ = \frac{Fuel\ Mass\ flow\ rate * rev/cycle}{revolutions\ per\ minute * number\ of\ cylinders} \quad \text{(Eqn. 5)}$$

To match the simulation fuel mass per cylinder per cycle with the data, the intake pressure and temperature are adjusted, therefore changing the amount of fuel trapped in the cylinder. These adjustments also change the in-cylinder pressure. Moreover, it is also crucial to match the pressure inside the cylinder at spark timing to the given data. This is an iterative process that takes several cycles to closely match all parameters. Figure 20 highlights some of the iterations completed to match the trapped mass of fuel.

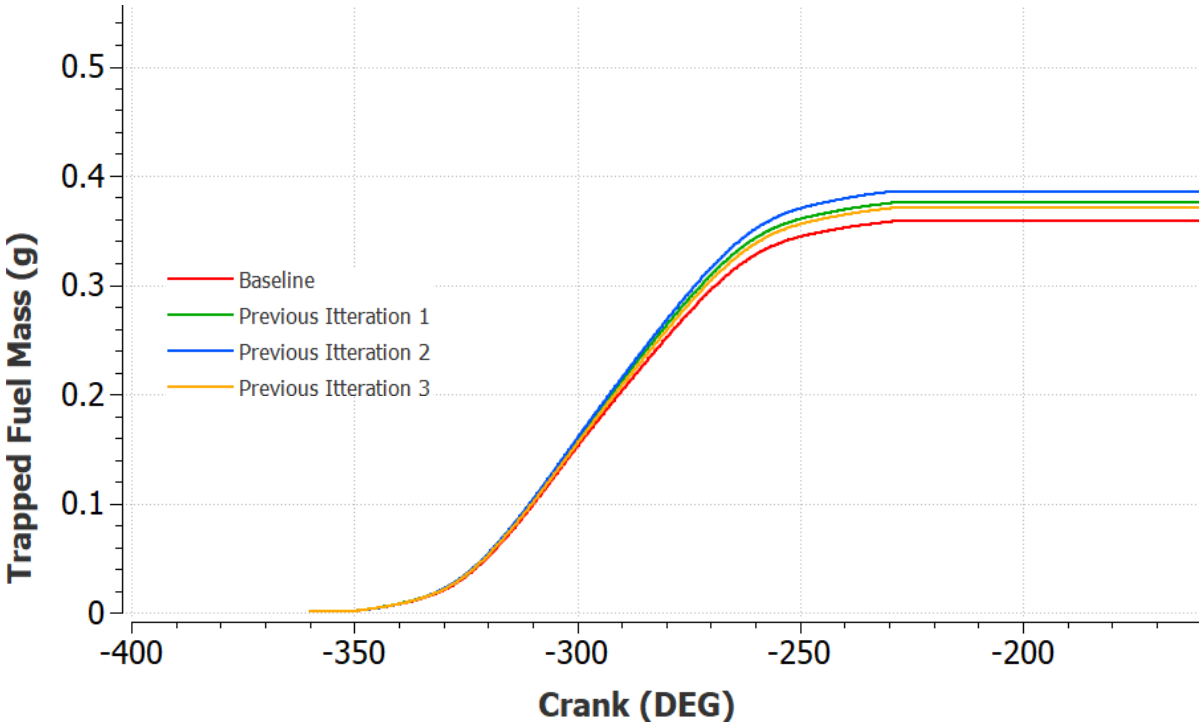

Figure 20. Pressure vs. crank angle emphasizes some of the iterations taken to match the trapped fuel mass.

The next step is to use the fuel mass per cylinder per cycle and equivalence ratio (with assumed natural gas composition), to calculate the mole fractions of the intake.

From this step, the mass fractions of the gas are calculated and put directly into Converge CFD in the form of another boundary condition.

The Converge CFD engine model is then utilized to obtain a motor trace. A motor trace is a pressure vs crank angle curve where no combustion occurs. This type of simulation is completed to get a base parameter for numerous values of the engine, as well as check the validity of the CFD model. This ensures that there are no basic errors such as meshing or mapping errors in the simulation. One of the key parameters of the motor trace is to obtain a baseline for pressure. This pressure baseline can be used to directly compare simulations that have suspected combustion. When comparing the pressures, a rise in peak pressure or a shift in the location of the peak pressure can provide some insight into whether or not combustion occurred. Figure 21 shows this peak-pressure shift when comparing the motor trace to a simulation that confirmed combustion.

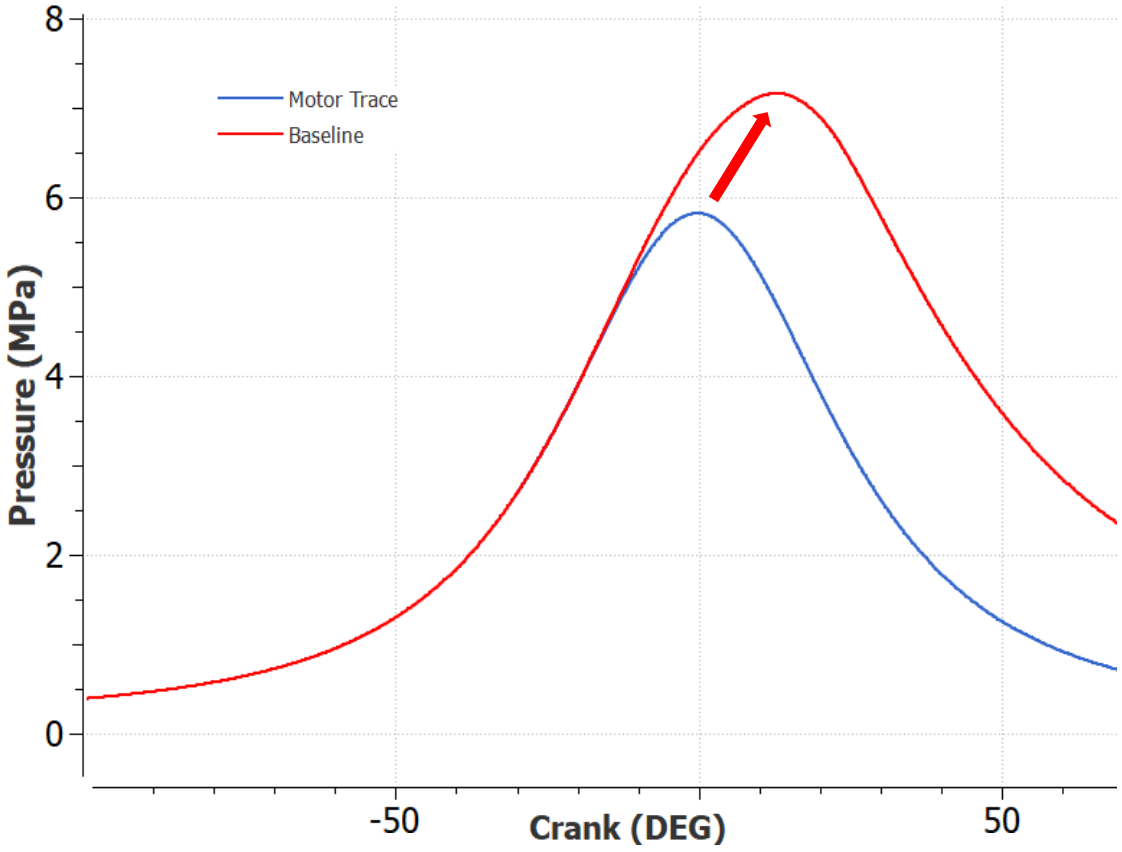

Figure 21. Pressure vs. crank angle emphasizes the difference between a simulation with combustion and the motor trace.

The brake work and power of the engine simulations are then used to further tune the baseline model. The brake work and power can be directly compared to engine data. Equation 6 is used to effectively calculate the amount of brake work provided by a simulation.

$$W = \int P dV \qquad \text{(Eqn. 6)}$$

W is the brake work produced from the simulations, P is the pressure of the cylinder and V is the Volume of the cylinder at a given crank angle. This work is considered indicated work as mechanical losses of the system are not considered. This

equation takes the pressure and volume data produced in the simulations and provides an amount of indicated work produced from the cycle. Equation 7 is then used to convert the brake work calculation into a unit that is also comparable to the physical engine.

$$P = \frac{W * RPM}{n * 60} \quad \text{(Eqn. 7)}$$

P is the indicated power of the engine, W is the indicated work of the simulation, RPM is the revolutions per minute, and n is the number of revolutions per cycle.

2.3.3 Peak Pressure Tunning

It became apparent that after running multiple simulations, the peak pressures of the baseline simulation do not sufficiently match the data and are closer to the motor trace, indicating minimal combustion. One strategy to mitigate this is to increase the compression ratio. To slightly increase the compression ratio, the piston is moved slightly up. The piston is raised by 1.5mm, increasing the compression ratio by 0.55. This ultimately has the effect of raising the pressure to match the data more closely.

Although it is closer, the pressure is still too low at this point. The mechanisms are assessed again using the previously mentioned study. Figure 22 highlights a mechanism's impact on combustion. From this figure, it is clear that there are significant differences in peak pressure, as well as the location of the peak pressure. The mechanism closest to the data in terms of peak pressure and location of peak pressure is the GRI 3.0 mechanism.

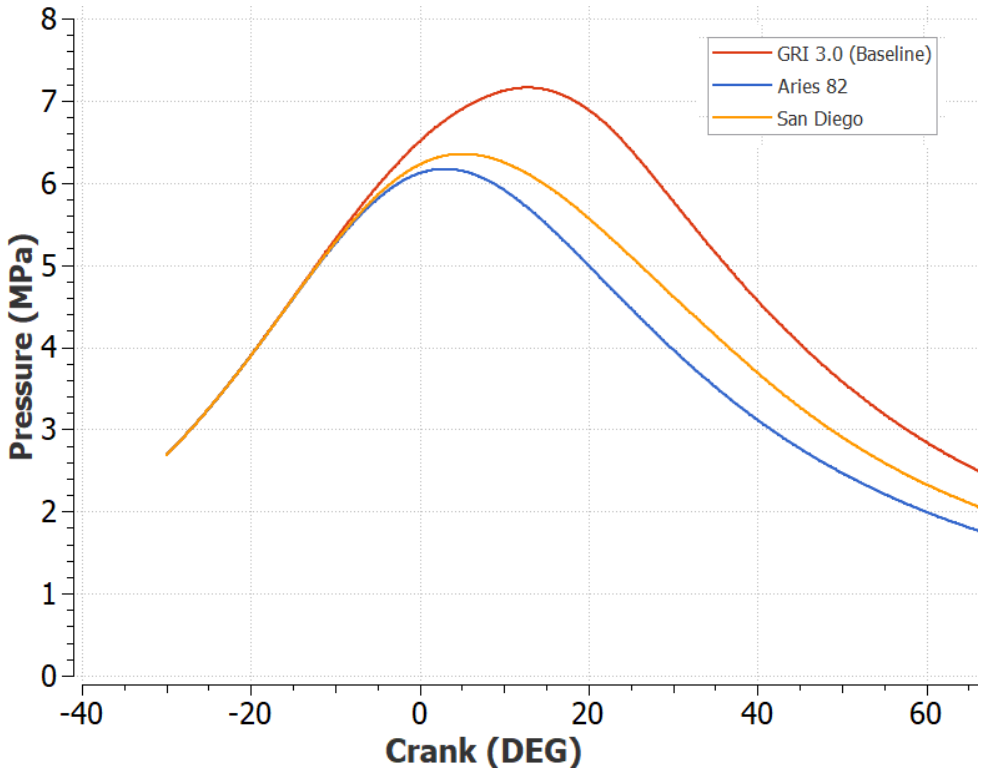

Figure 22. Pressure vs. crank angle emphasizes the difference between a simulation with combustion and the motor trace.

From this point, the peak pressure is occurring earlier than the data. The next step in this research used to tune the baseline is to adjust the Prandtl number. The Prandtl number is a ratio of the momentum diffusivity to thermal diffusivity of the fuel and air mixture. The initial simulations had a Prandtl number of 1, signifying that there is not a dominating effect from either the momentum or thermal transfer. The Prandtl number is lowered to 0.9 for the baseline, allowing for the thermal diffusivity of the fuel and air to be slightly more dominant than momentum diffusivity. With this modification, the transfer of heat through the gas produces a more significant effect. Figure 23 displays the differences in peak pressure stemming from adjustments to the Prandtl number, highlighting a slight increase in peak pressure and a late shift in the location of the peak pressure.

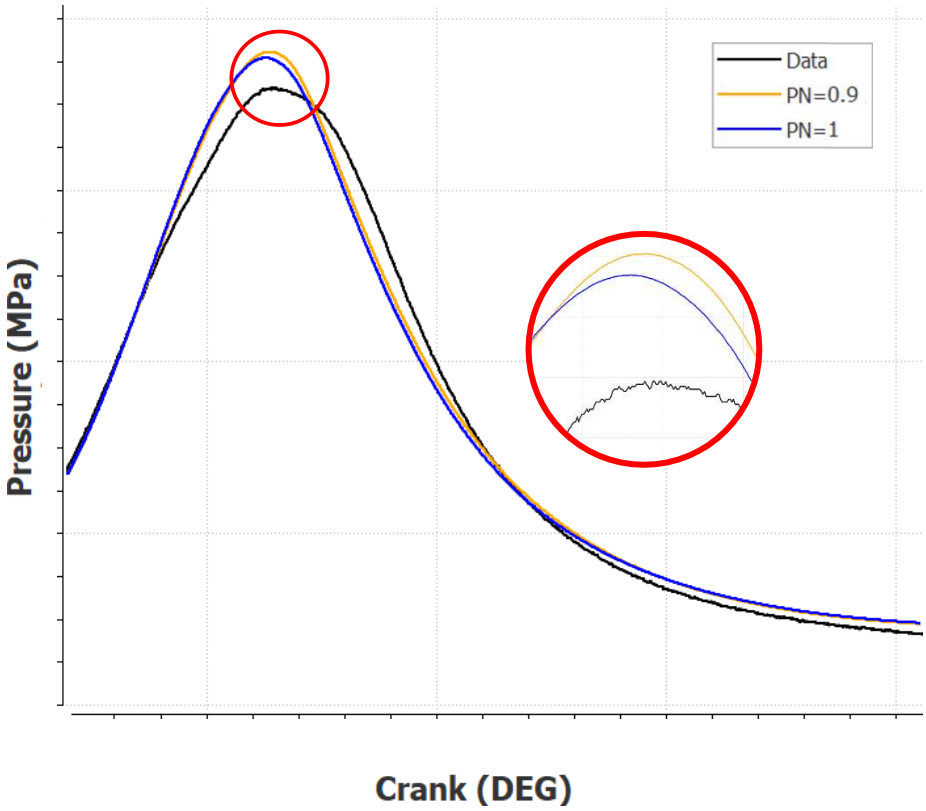

Figure 23. Pressure vs. crank angle emphasizes the difference between a simulation with combustion and the motor trace.

To complete the baseline, it is essential to address the peak pressure occurring in levels significantly higher than that of the data. This discrepancy is suspected to have occurred because the GRI mechanism is overpredicting the combustibility of the fuel and air occurring inside the simulation. To mitigate this, the reaction rate multiplier is adjusted to control how fast the combustion reaction is occurring. In this research, the reaction rate multiplier is adjusted from 1.0 to 0.9 to lower the peak pressure. This allowed the peak pressure and location of peak pressure to be acceptable for the baseline simulation. The results from the baseline will be discussed in the following chapter.

2.4 End Gas Auto-Ignition

When inducing end gas auto-ignition, it is important to analyze the ignition delay of the fuel. Figure 24 emphasizes that ignition delay decreases as temperature goes up.

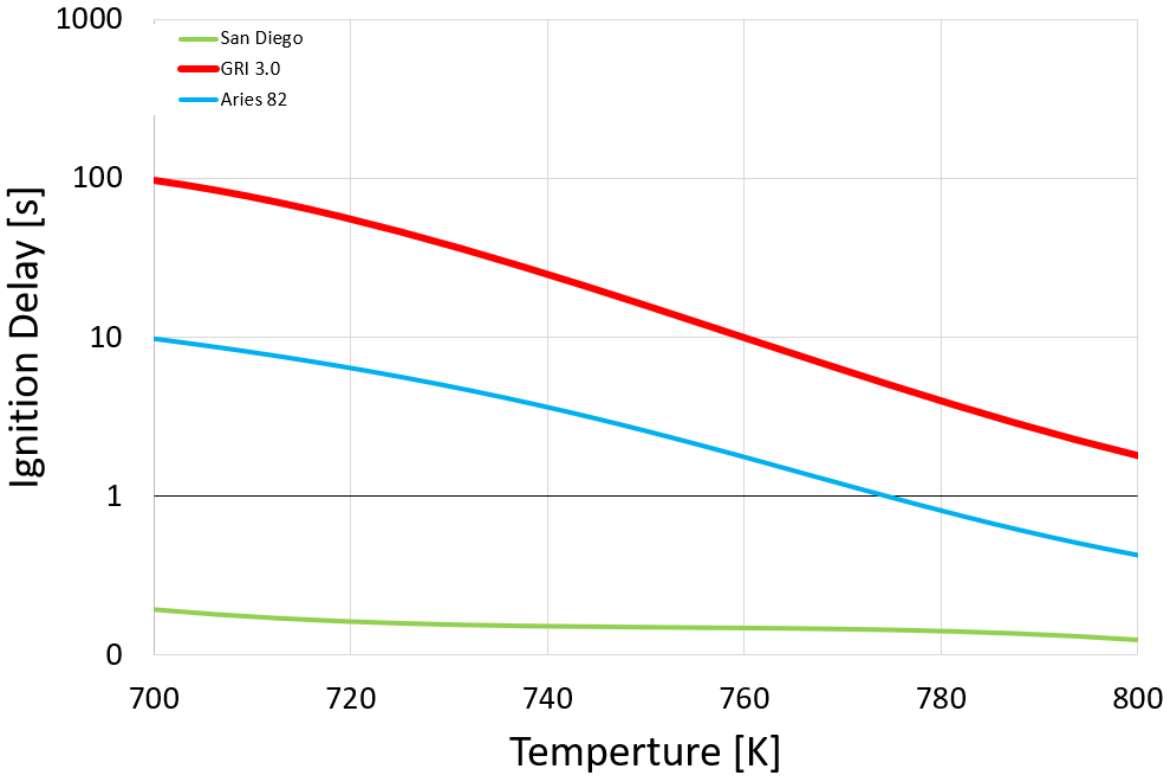

Figure 24. Ignition delay vs. temperature for different mechanisms.

This relationship indicates that the fuel in the engine will be more likely to auto-ignite if the temperature or pressure increases. To increase temperature and pressure in the cylinder, a fundamental strategy is to advance the spark timing of the engine, i.e., setting the spark timing earlier in the combustion cycle. This will cause the fuel to ignite sooner and contribute to higher temperatures and pressures in the cylinder. The spark timing is advanced from its original timing of -30 degrees before top-dead-center to -50 by

increments of 2 degrees. This spark timing range allows for the assessment of EGAI and offers insight regarding potential auto-ignition in the G3516J engine.

2.5 Hydrogen Blending

Because natural gas is mainly comprised of methane, the flame speed of the natural gas is relatively slow. To increase the flame speed of natural gas, other fuels with higher flame speeds can be added. This project utilizes the addition of hydrogen in natural gas to increase the overall flame speed. The natural gas amount is lowered, and hydrogen is added to the fuel to maintain the same equivalence ratio and chemical energy of the trapped mass of fuel. The fuel blend combinations are 5%, 10%, 20%, and 30% hydrogen. The percentages of hydrogen are substituted by volume and used to calculate mass fractions of the fuel and air. These mass fractions are then inputted into the CFD simulations. After the results are collected from this methane emission reduction strategy, the intake manifold pressure is lowered to match the overall power for each gas mixture. Because hydrogen is more reactive, there is increased work and power generated for the various gas mixtures. Lowering intake pressure lowers the amount of trapped mass. This helps match the actual power produced by the simulations compared to the baseline. After the power is matched, the methane emissions are studied and compared across all simulations. This is also done with NOx emissions. When adding in hydrogen, there are higher temperatures associated with combustion. These higher temperatures translate to increased levels of NOx.

2.6 NOx Emissions

NOx mitigation strategies are also explored. This is done by adjusting the equivalence ratio and leaning out the gas mixture further. The same calculations that are done to find the mass fractions of the species entering the baseline are utilized to find the mass fractions of the species in the 30% H2 blend. The difference here is that the equivalence ratio is adjusted by decreasing the amount of fuel and increasing the amount of air that is entering the engine. This is done to decrease cylinder temperatures in an attempt to decrease NOx emissions.

CHAPTER 3- RESULTS

This chapter covers the results from this research, including baseline tuning, inducing end-gas auto-ignition, and emissions reduction resulting from hydrogen substitution matching energies from trapped fuel and matched indicated power. This chapter will also address a NOx emission reduction strategy using a representative gas mixture of 30% H2.

3.1 Baseline results

As discussed in the previous chapter, many criteria compared the baseline to engine data to consider the baseline tuned. The first of these criteria to match are the pressures of the simulation. The pressures included starting pressure, pressure at spark timing, and peak pressure. Figure 25 shows the baseline pressure curve in red. The grey curves compare the data captured from a physical engine. The baseline pressure curve lies towards the middle of the engine data pressure curves. Figure 26 isolates the representative curve from the data as well as the baseline simulation pressure curve to compare against the baseline.

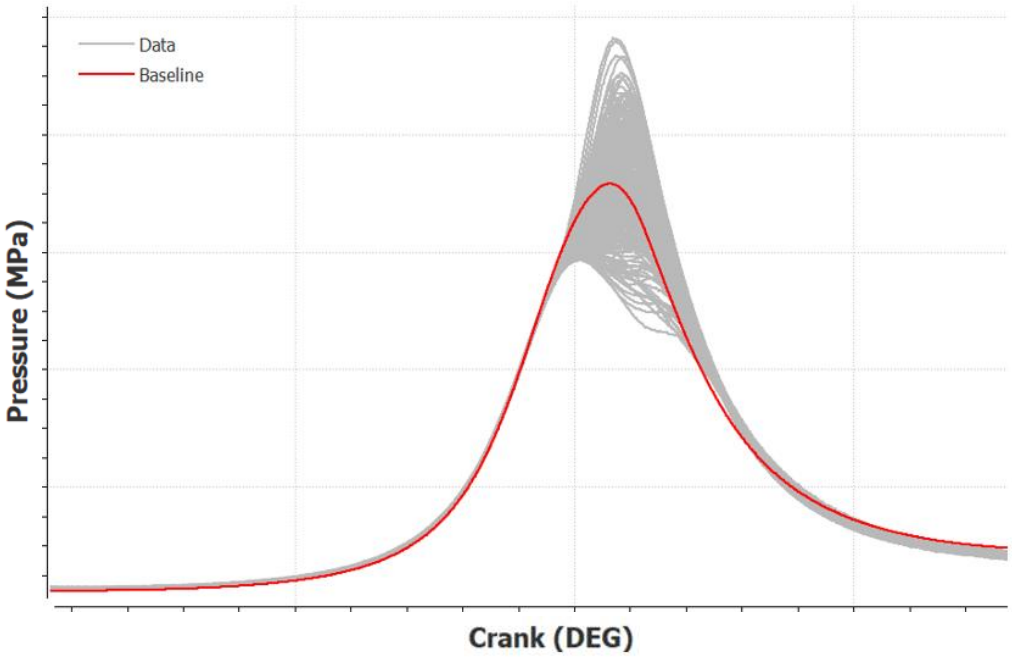

Figure 25. Pressure vs. crank angle for baseline and data.

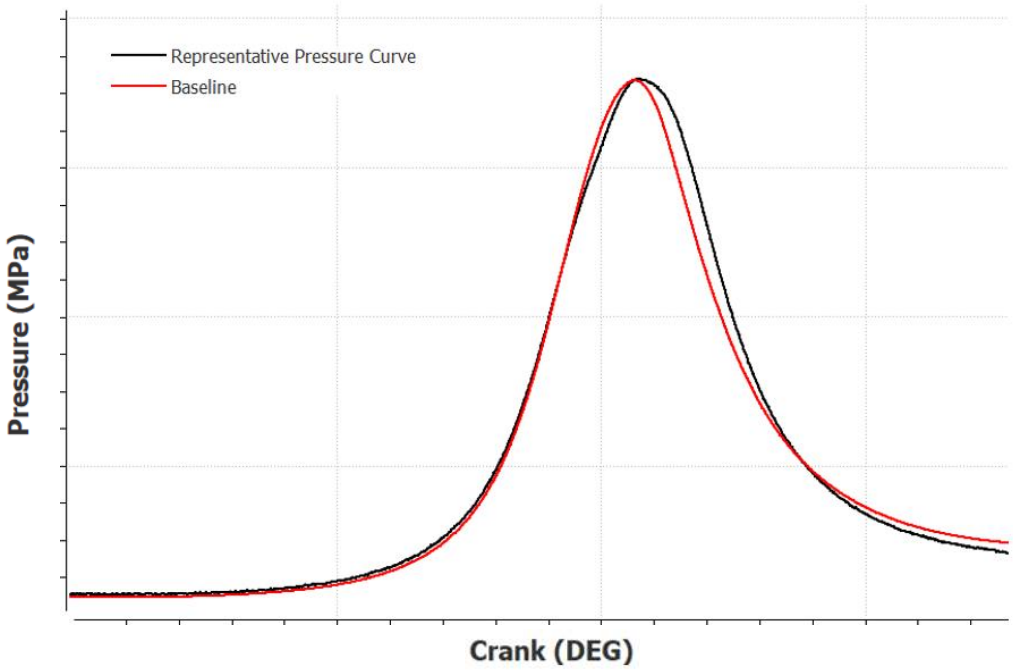

Figure 26. Pressure vs. Crank angle for baseline and representative data.

Another criterion to assess the baseline is the trapped mass of the fuel. Table 1 shows the value for the trapped mass and compares it to the engine data. This has about an 8% error. Even though this amount could be adjusted to lower the percent difference, it would severely impact the peak pressure and the location of the peak pressure. This is most likely due to the changing flame speeds that occur with lower pressures. The equivalence ratio also could not have been reduced to match the trapped mass of fuel because this would also affect the peak pressure due to a change in the fuel combustibility. Table 1 also contains the rest of the criteria used to determine the baseline model tuning, such as ER, indicated power, and peak pressure, with percentage differences of 1.30%, 0.43%, and 0.42%, respectively. The numerical values for the criteria are excluded for confidentiality reasons.

Table 1. Baseline tuning criteria

	Percent Difference
Pressure at CA -360 [MPa]	4.03%
Pressure at CA -30 [MPa]	2.84%
Peak pressure [MPa]	0.42%
Location of Peak pressure [Degree]	8.06%
Trapped mass of fuel [kg]	8.15%
Equivalence Ratio	1.30%
Indicated Work [Nm]	0.44%
Indicated Power [kW]	0.43%

After the baseline is accepted, preliminary data is gathered from the simulation and compared to the following experimental simulations. For example, the amount of CH4 left unburned before the exhaust valves are opened is used to assess the methane emission reduction strategies. Figure 27 shows a graph of CH4 inside the cylinder of the simulation over various crank angles. It shows the trend where the exhaust valves are opened, and the fuel enters, causing a rise in the trapped CH4. The exhaust valves then close, and the amount of CH4 levels out. Following this, the combustion begins at CA -30, and the amount of trapped CH4 decreases until the exhaust valves are opened. This data gives a value for the trapped mass of CH4 for the baseline and the amount left unburned.

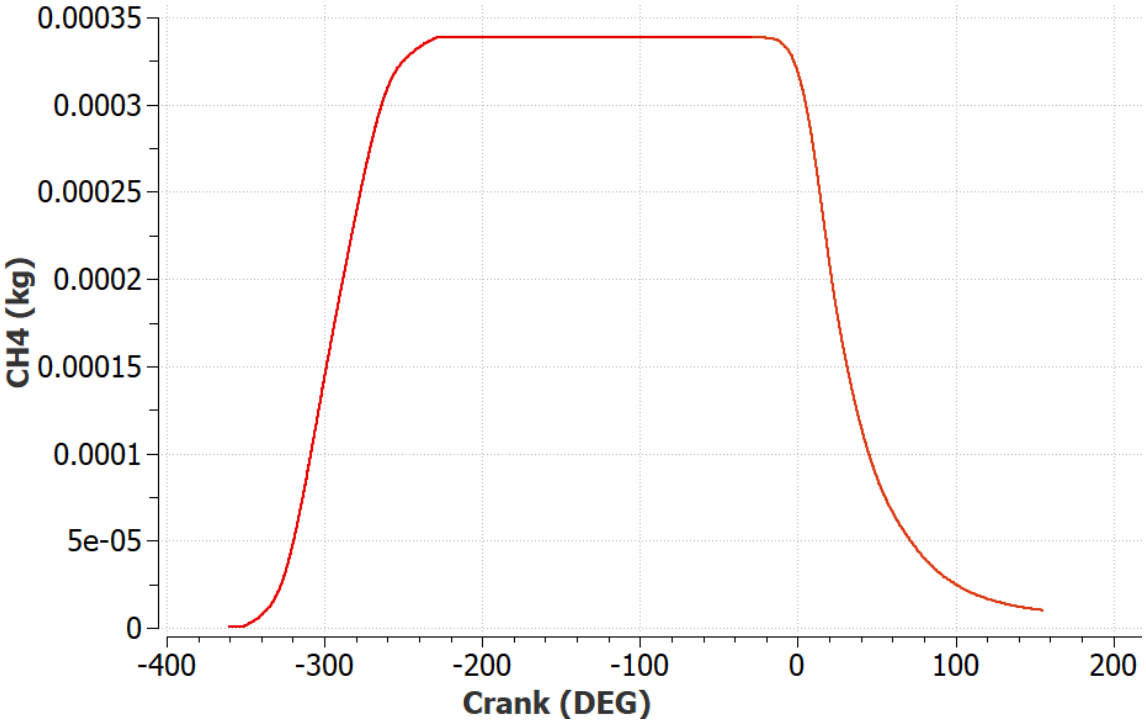

Figure 27. Trapped CH4 vs. crank angle for baseline simulation.

Figure 28 and Figure 29 are used to directly compare where there are areas of unburned fuel post-combustion. They are also used to analyze combustion and compare how various changes affect the combustion at given crank angles. Figure 28 shows the

mass fraction of CH4 inside the cylinder at spark timing, top-dead-center (TDC), the midpoint between TDC and exhaust valve opening, as well as right before the exhaust valves are open. The red areas are the areas that contain the highest mass fractions of CH4, and the blue areas are the already combusted fuel and air that has relatively no CH4 remaining. The CA155 image in Figure 28 shows that most unburned CH4 resides in or near the crevice volume. Figure 29 depicts the same mass fraction of methane but utilizes two cross-sectional areas to better examine the crevice volume and how the combustion acts as it approaches.

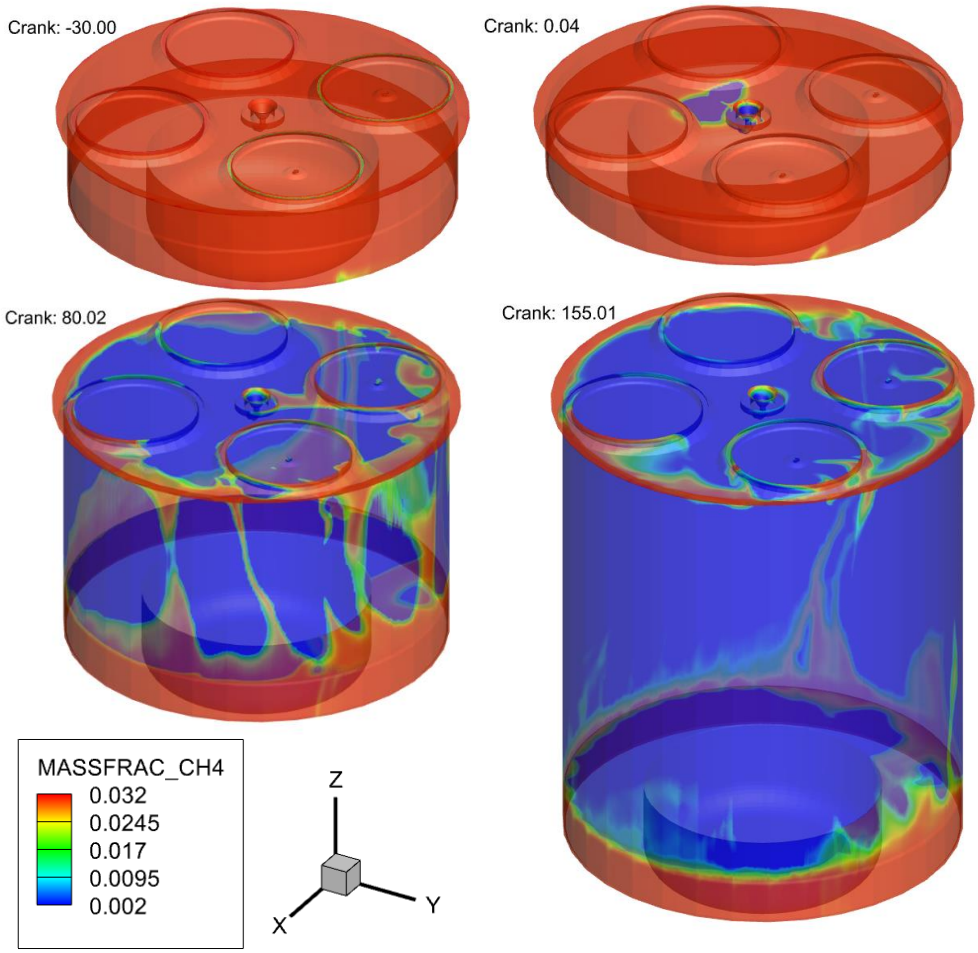

Figure 28. 3D rendering of CH4 mass fraction at various crank angles.

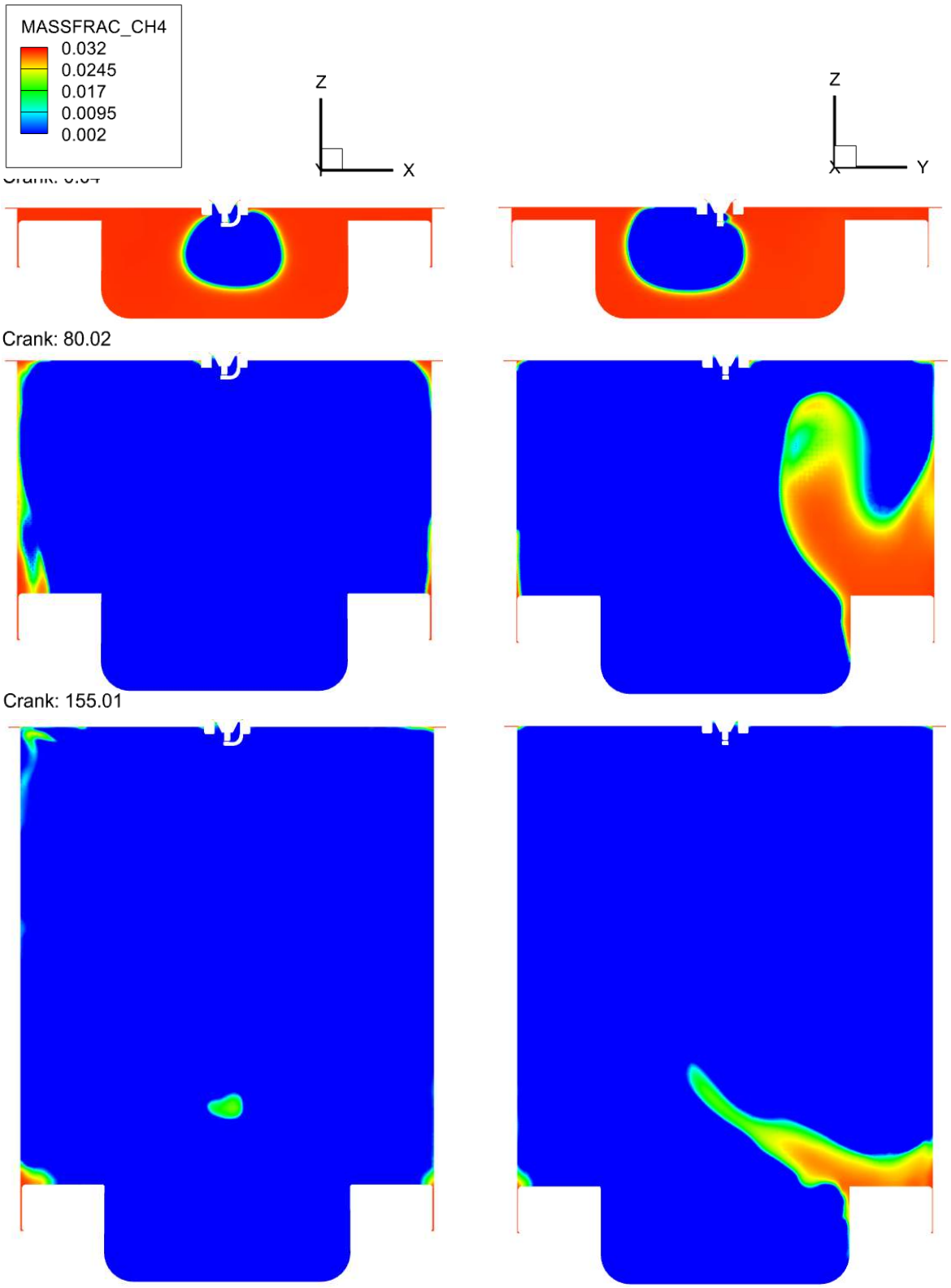

Figure 29. Cylinder cross sections depict CH4 mass fraction at various crank angles.

The second image of the first row in Figure 29 depicts the combustion heading in a particular direction. This is due to the velocity fields that occur in the simulation. Figure 30 depicts the velocity fields of the baseline and highlights the velocities pointing to the left of the image near the spark plug. This ultimately pushed the combustion in that direction. The same velocity vectors also cause the large unburned CH4 area near the bottom right of the last image in Figure 29 to move to the left of the image, towards the center of the chamber. The velocity field swirled in such a way that this area was the last to burn. Figure 31 shows the velocity vectors for various crank angles leading to the exhaust valves opening, effectively ending combustion, and leaving unburned CH4.

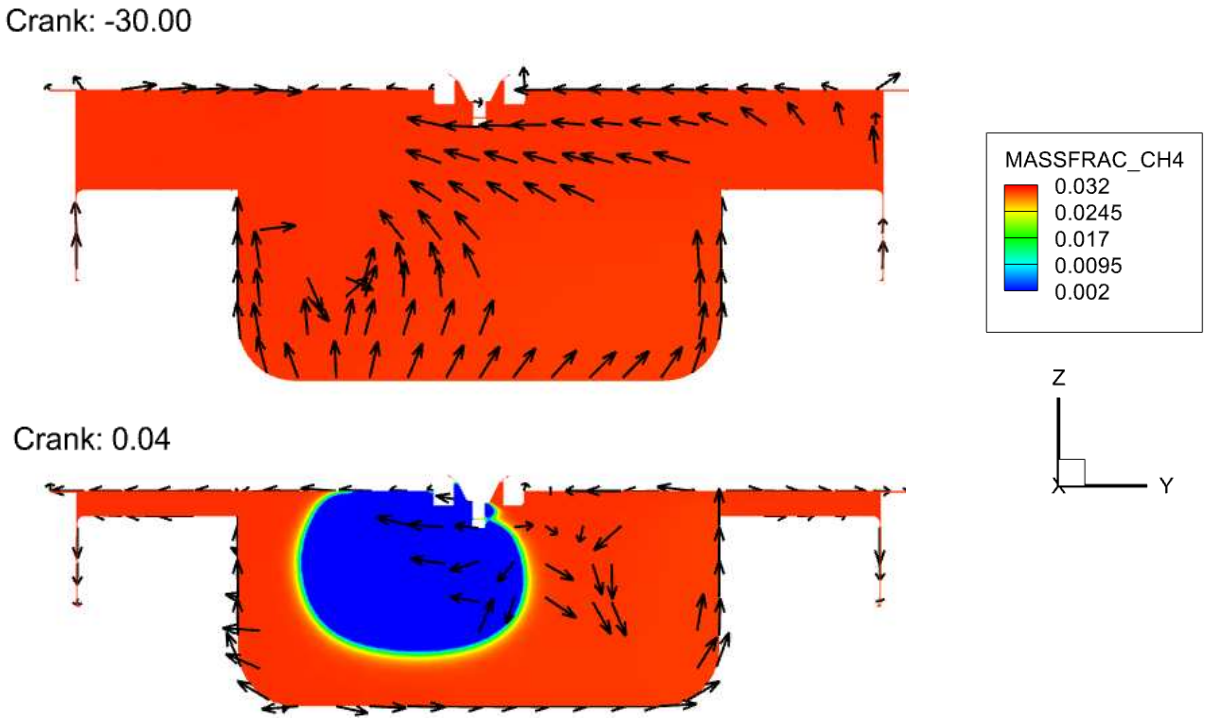

Figure 30. Cross sections of cylinder depicting mass fraction of CH4 and velocity vectors.

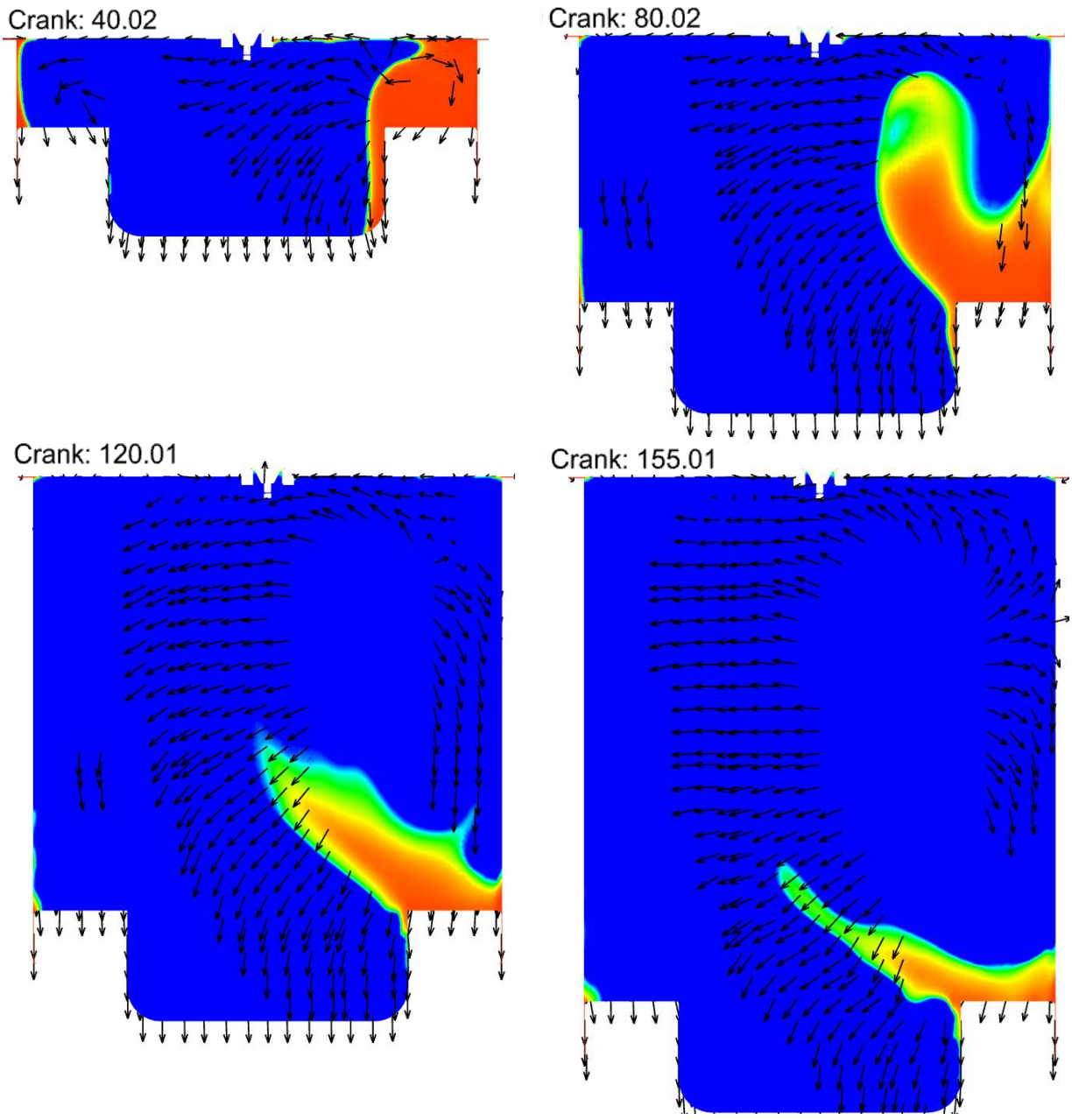

Figure 31. Cross sections of cylinder depicting mass fraction of CH4 and velocity vectors.

3.2 End Gas Auto-Ignition Results

The strategy used in this research to induce EGAI is to advance the spark timing by increments of 2 crank angle degrees. The pressure vs. crank angle graphs from these simulations can be seen in Figure 32. The peak pressures steadily increase as the spark timing is advanced. This higher peak pressure translated to lower CH4 emissions up until CA -40. After this, there is an increase in unburned CH4. Table 2 contains the unburned CH4 values for the various spark timings. The trend of unburned CH4 is highlighted in Figure 33. Based on the amounts of unburned CH4, a spark timing of CA -40 would yield the lowest amount. More spark advancement would continue to raise the peak pressure but yield more unburned CH4.

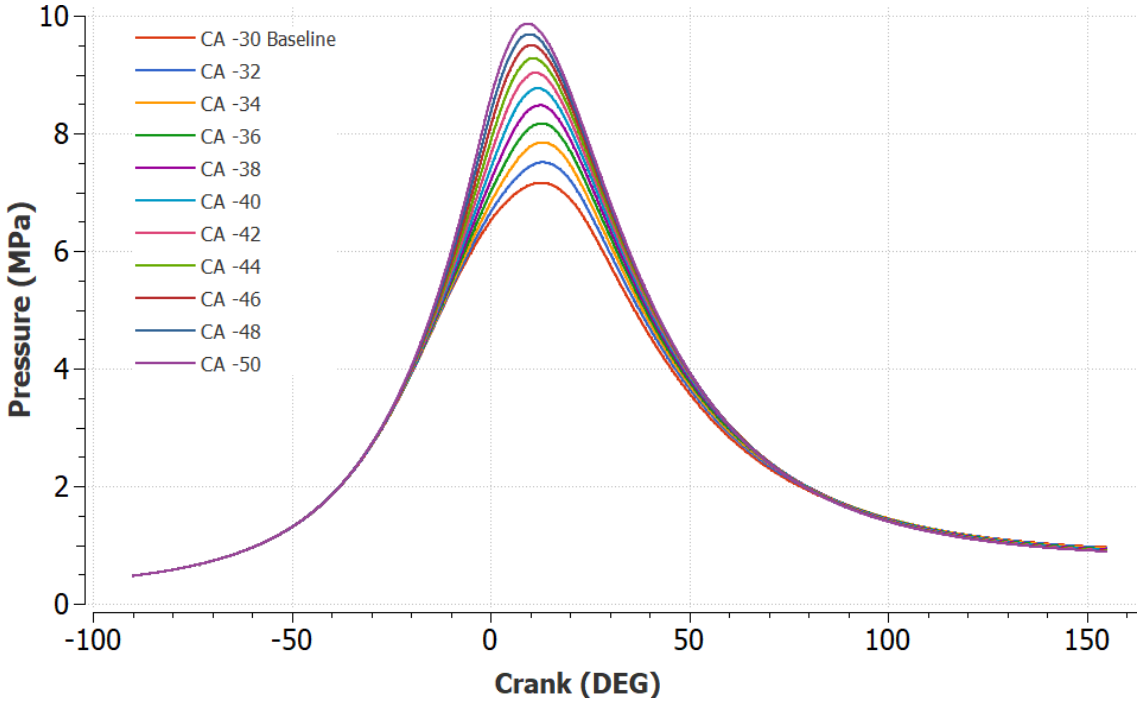

Figure 32. Pressure vs. crank angle for various spark timings.

Table 2. Trapped CH4, unburned CH4, and unburned percentage for various spark timings.

	Trapped CH4 [kg]	Unburned CH4 [kg]	Unburned Percentage
Baseline	0.000338348	1.01406E-05	3.00%
CA -32	0.000338348	8.05221E-06	2.38%
CA -34	0.000338348	7.69248E-06	2.27%
CA -36	0.000338348	7.69248E-06	2.27%
CA -38	0.000338348	7.65300E-06	2.26%
CA -40	0.000338348	7.64890E-06	2.26%
CA -42	0.000338348	7.80393E-06	2.31%
CA -44	0.000338348	8.08009E-06	2.39%
CA -46	0.000338348	8.23617E-06	2.43%
CA -48	0.000338348	8.59427E-06	2.54%
CA -50	0.000338348	8.87078E-06	2.62%

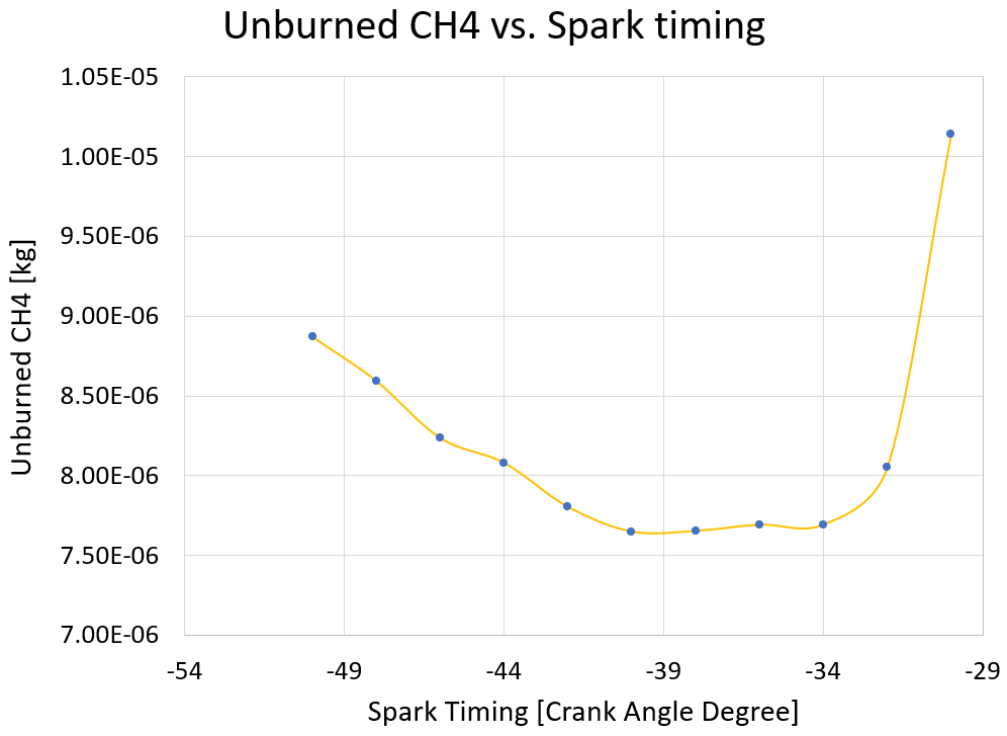

Figure 33. Unburned CH4 vs. spark timings.

Although there appears to be a trend that shows a reduction of unburned methane as the spark timing is advanced, it is not evident that there are any signs that EGAI is the cause. When EGAI occurs, pressure waves separate from the primary combustion are formed. These pressure waves collide with the original pressure waves from the spark plug combustion. When this happens, pressure spikes typically appear on the pressure curves. When analyzing Figure 30, there are no pressure spikes visible. Another piece of evidence to support this claim can be seen in Figure 34. In this figure, the mass fractions of CH4 are observed at various crank angles. Because ignition delay is lower for higher temperatures and pressures, CA 9 and CA 35 are depicted. These images are taken at the peak pressure and temperature, respectively. Two more CA images are also shown after these two events, but none show evidence of EGAI. It would be expected that if EGAI occurred, the high concentration of CH4 (red areas) would combust separately from the main combustion. Because of this, under the given engine conditions, there appears to be no evidence that advancing the spark timing will induce EGAI. It can also be surmised that advancing spark timing can still lower the amount of unburned CH4, most likely due to increased pressures and faster flame speeds.

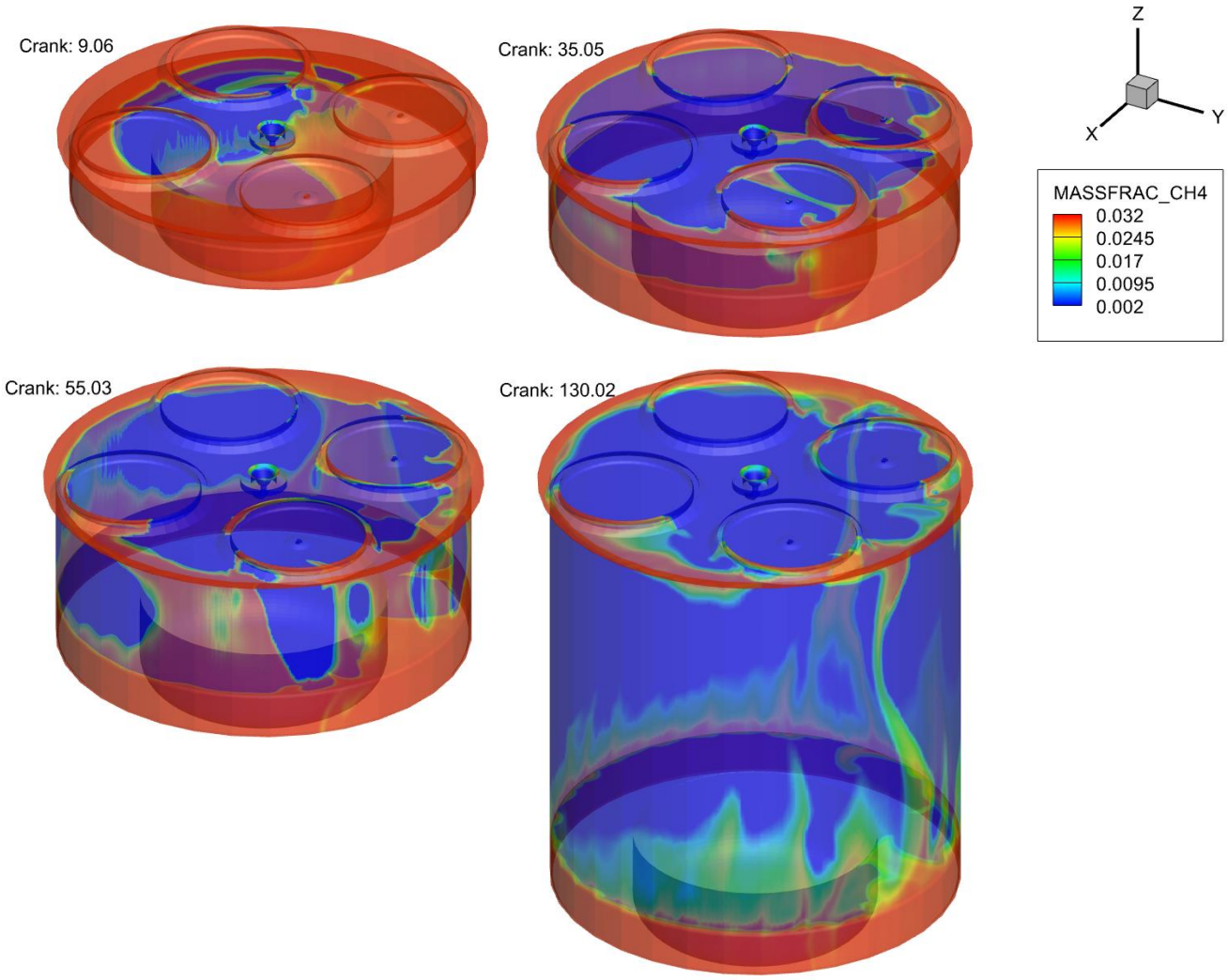

Figure 34. Mass Fraction of CH4 for spark timing of CA -40.

3.3 Hydrogen blending results for chemical energy matched simulations.

The following experiment discussed in this chapter is the blending of hydrogen. This section will focus on 5%, 10%, 20%, and 30% hydrogen blends by volume. This section includes the results for maintaining the same equivalence ratio and the same chemical energy that the trapped mass of fuel and air contains. This is done to directly compare the reactivity of the substituted hydrogen to natural gas fuel.

The first step is to calculate the mass fractions of fuel after the substitution by volume. Then, the intake pressure is adjusted to reflect the correct amount of fuel mixture to match the chemical energy of the baseline. This resulted in lower intake manifold pressures for all the gas mixtures except for the 5% H2 blend. This is likely due to the more significant effect of the lower density of hydrogen allowing less fuel into the system. Table 3 shows the intake pressures for the different gas mixtures and the mass of the fuel trapped in the cylinder for the closest cases. This table also contains the percentage differences for the trapped mass values. After the trapped masses are matched, the intake portion of the simulations is accepted. The combustion cycles are run with the mapping files created from these intake cycles. Figures 35 and 36 depict methane and hydrogen mass fractions over various crank angles. These figures highlight the differences gas mixtures have. For example, in Figure 35, the amount of CH4 decreases from the baseline amount as there is more hydrogen substitution. The opposite trend can be seen for hydrogen in Figure 36, where the baseline has no hydrogen substitution.

Table 3. Trapped CH4, unburned CH4, and unburned percentage for various H2 Blends.

	Intake Pressure [kPa]	Trapped CH4 [g]	Unburned CH4 [g]	Trapped CH4 reduction from baseline	Unburned CH4 reduction from baseline
Baseline	450	0.338496	0.0101406	NA	NA
5% H2	451	0.334335	0.005623	1.23%	44.55%
10% H2	449	0.327335	0.00459957	3.30%	54.64%
20% H2	447	0.314036	0.00452905	7.23%	55.34%
30% H2	446	0.299364	0.00333835	11.56%	67.08%

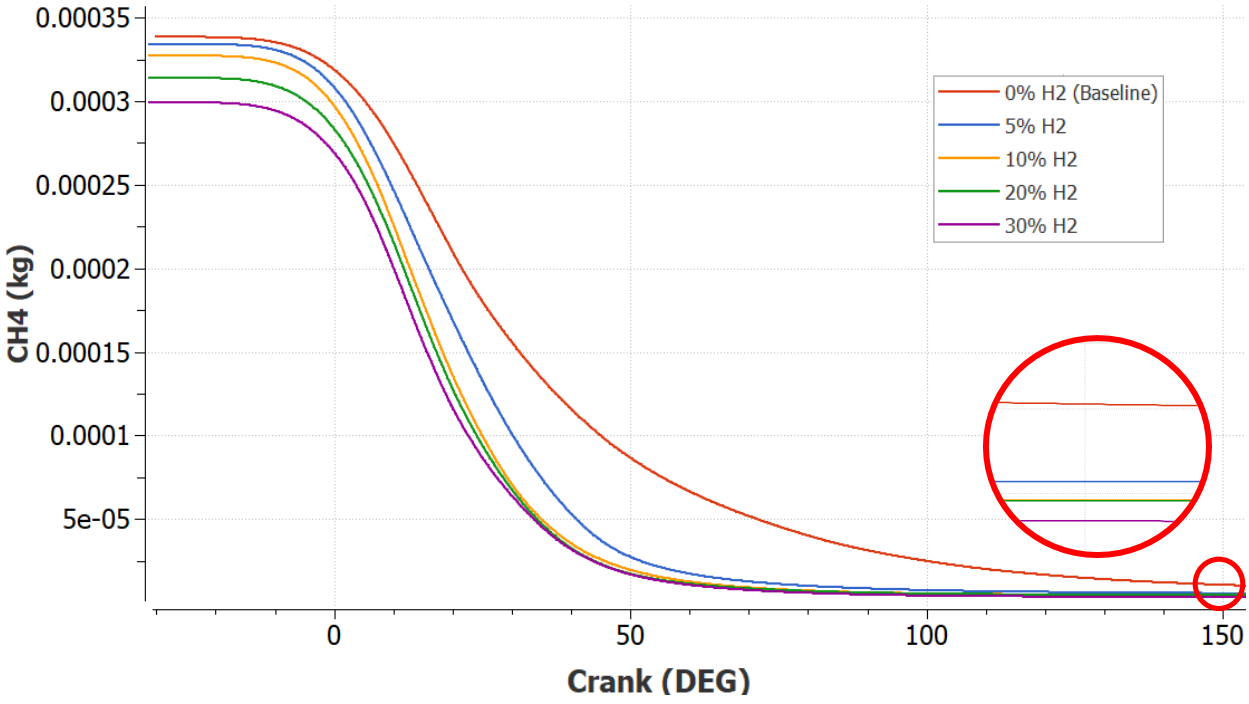

Figure 35. Trapped CH4 vs. Crank angle for various gas blends.

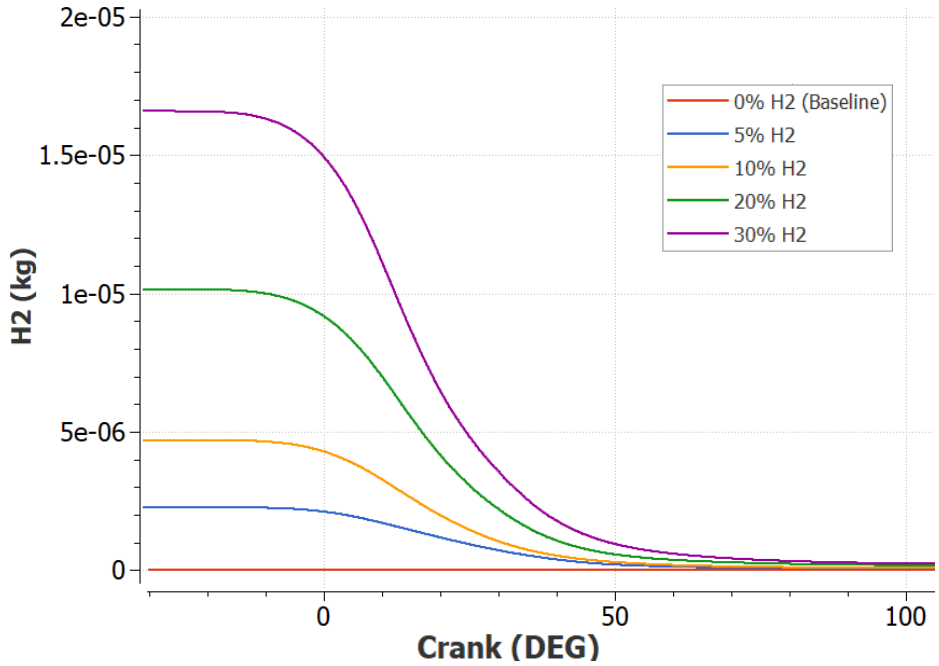

Figure 36. Trapped hydrogen vs. crank angle for various gas blends.

Table 3 shows the numerical results for the unburned methane from each gas mixture compared to the baseline. This table includes the percentage unburned compared to the trapped mass of methane for each gas mixture and shows the amounts of CH4 at CA 155 are lower for increasing amounts of hydrogen substitution. This table also consists of the percentage difference between the trapped amount of CH4 for the baseline compared to each gas mixture. Finally, the table includes the percent difference for the unburned CH4. These percentage differences are compared to prove the validity of the gas mixtures. For example, the 30% H2 Blend has a decrease in trapped mass of CH4 by 11.56%. The percent unburned relative to the baseline is 67.08%, leading to the conclusion that the reduction of unburned CH4 is caused by the substitution and increased combustion efficiency. This trend can be seen for every H2 gas mixture. Figure 37 shows the 3D plots for the mass fraction of CH4 at CA155 for the baseline and 30% H2 blend. Red circles highlight significant differences between the simulations. Figure 38

shows mass fractions of CH4 amounts in cross-sectional areas of the cylinder. It highlights the crevice volume of the cylinder for the baseline, 10% H2 Blend, and 30% H2 Blend. From this figure, it can be seen that the flame propagates closer to the crevice volume and the cylinder wall. The higher temperatures experienced with the H2 substitution most likely assisted in mitigating the wall quenching.

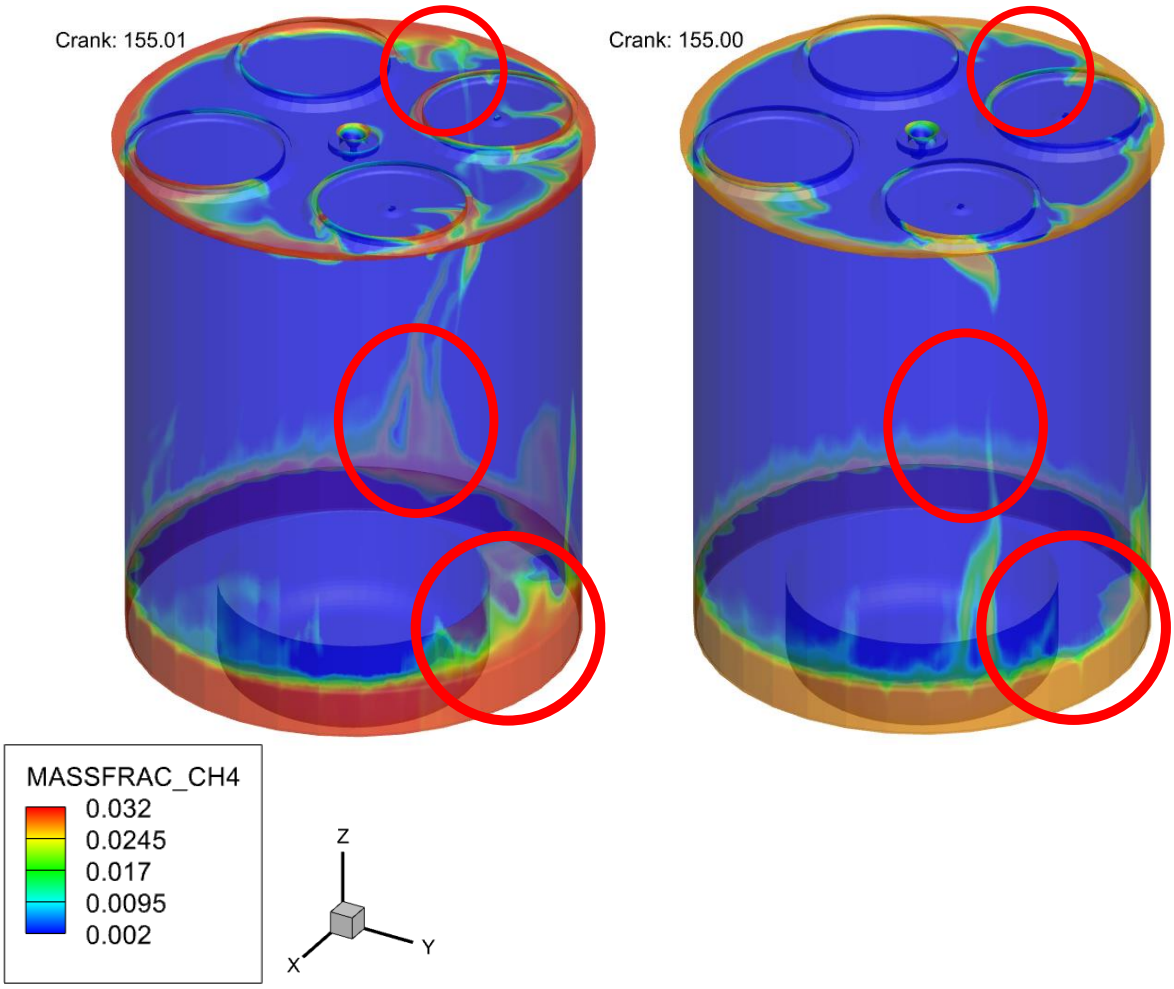

Figure 37. Mass fraction of CH4 at CA 155 for baseline simulation and 30% H2 fuel.

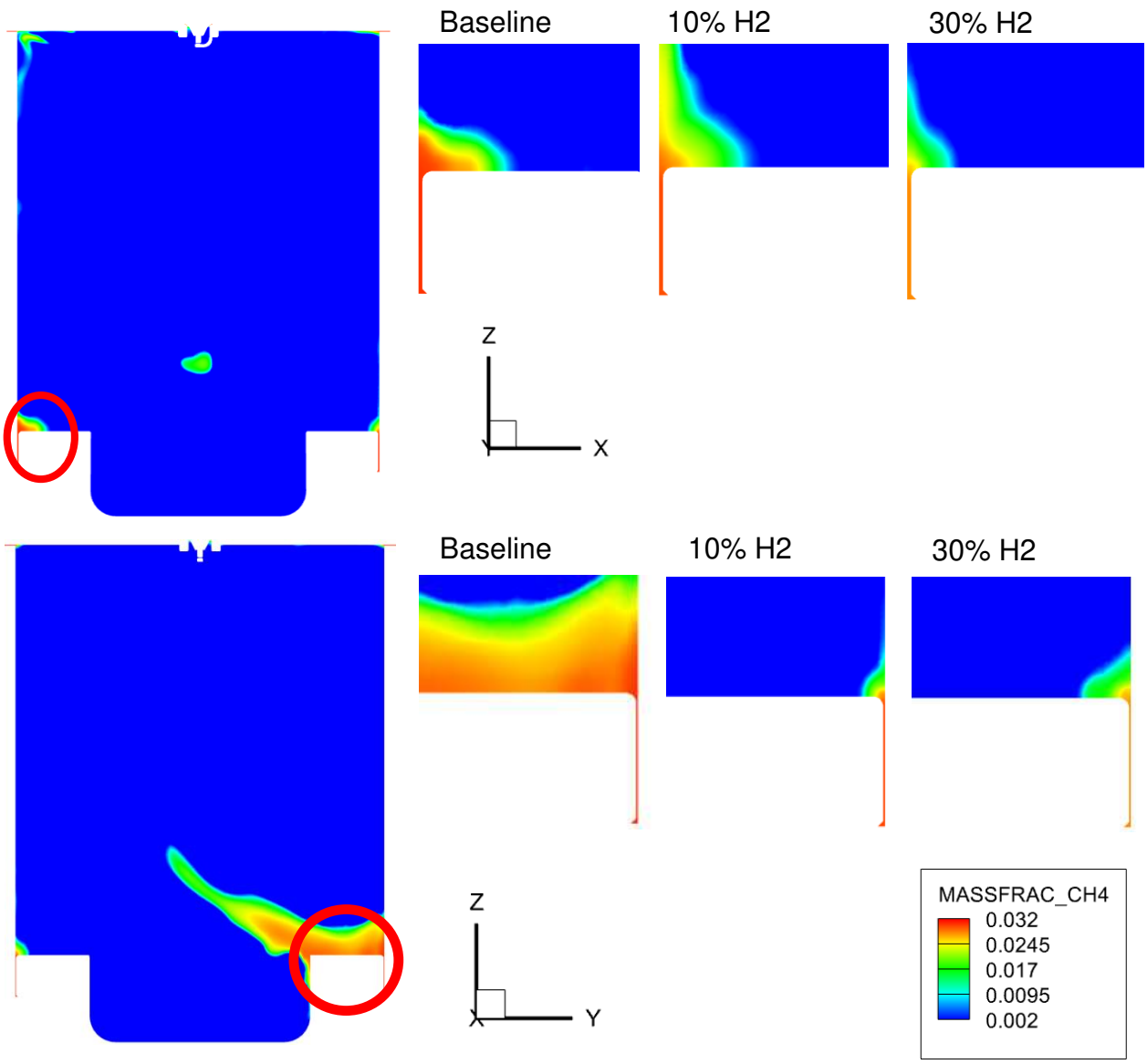

Figure 38. Cylinder cross sections depict CH4 mass fraction at various crank angles emphasizing the crevice volume.

By substituting natural gas with hydrogen, the flame speed of the gas mixtures increases. This leads to more fuel being burned during combustion at the same engine speed. Table 4 shows the flame speeds based on gas composition, temperature, and pressure at spark. It highlights that as the percentage of hydrogen substitution increases, the flame speed also increases despite the adjustment to match chemical energy.

Table 4. Flame speeds for each chemical energy-matched gas mixture based on conditions at spark.

	Pressure [MPa]	Temperature [K]	Equivalence ratio	Flame Speed [m/s]
Baseline	2.687	654.7	0.61	0.172
5% H2	2.695	655.2	0.61	0.175
10% H2	2.685	655.5	0.61	0.180
20% H2	2.677	655.8	0.61	0.191
30% H2	2.680	656.9	0.61	0.204

The combustion pressure curves from these gas substitutions can be seen in Figure 39. These show higher peak pressure values than the baseline for all gas mixtures. Due to the higher in-cylinder pressures, the indicated power produced from each gas mixture is higher than the baseline. Because of this, the power output for each gas substitution is matched to the baseline, and the CH4 emissions are reassessed in the next section.

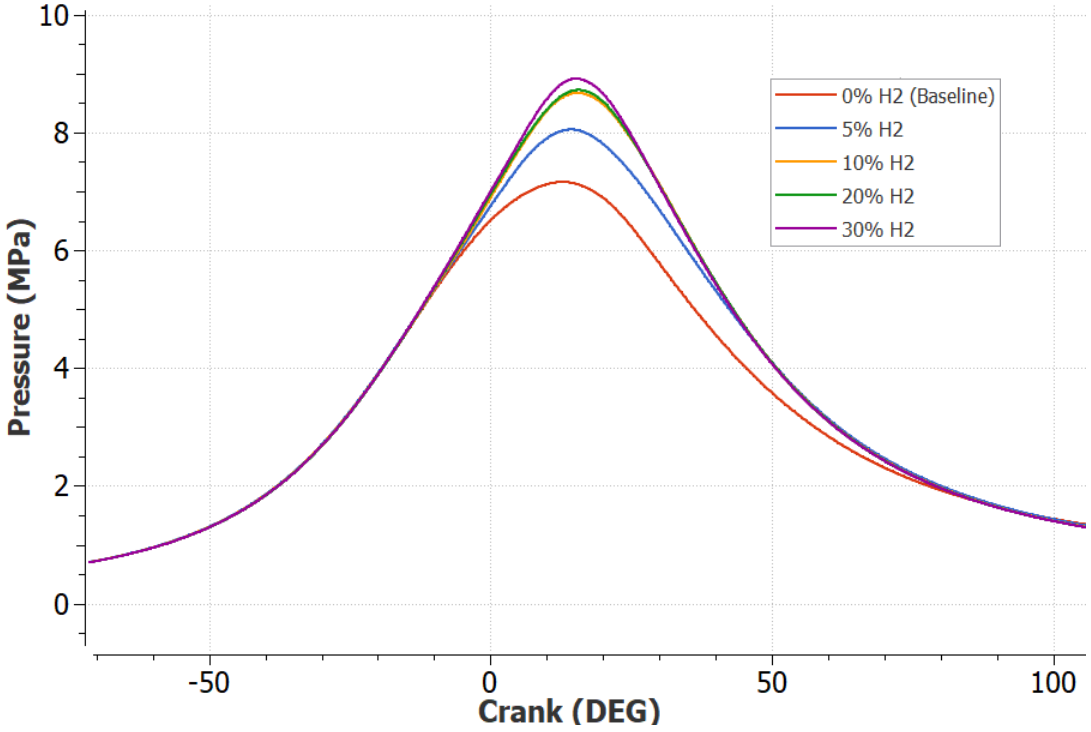

Figure 39. Pressure vs. crank angle for various gas blends.

3.4 Hydrogen Blending Results for Indicated Power Matched Simulations.

The final step for this research is to see the effects of hydrogen substitution on methane emissions for indicated power-matched gas mixtures. This is done by substituting hydrogen by lowering the other fuels in the natural gas mixture, similar to the previous section. The intake manifold pressure is then reduced until the correct amount of fuel is trapped inside the cylinder to produce an equivalent amount of indicated power to the baseline. Figure 40 depicts the pressure curves that are produced from this process. This figure shows the analyzed gas mixtures and highlights the pressures at the start of combustion. The red circle in the figure depicts an enhanced view showing the effect of decreasing the intake pressure.

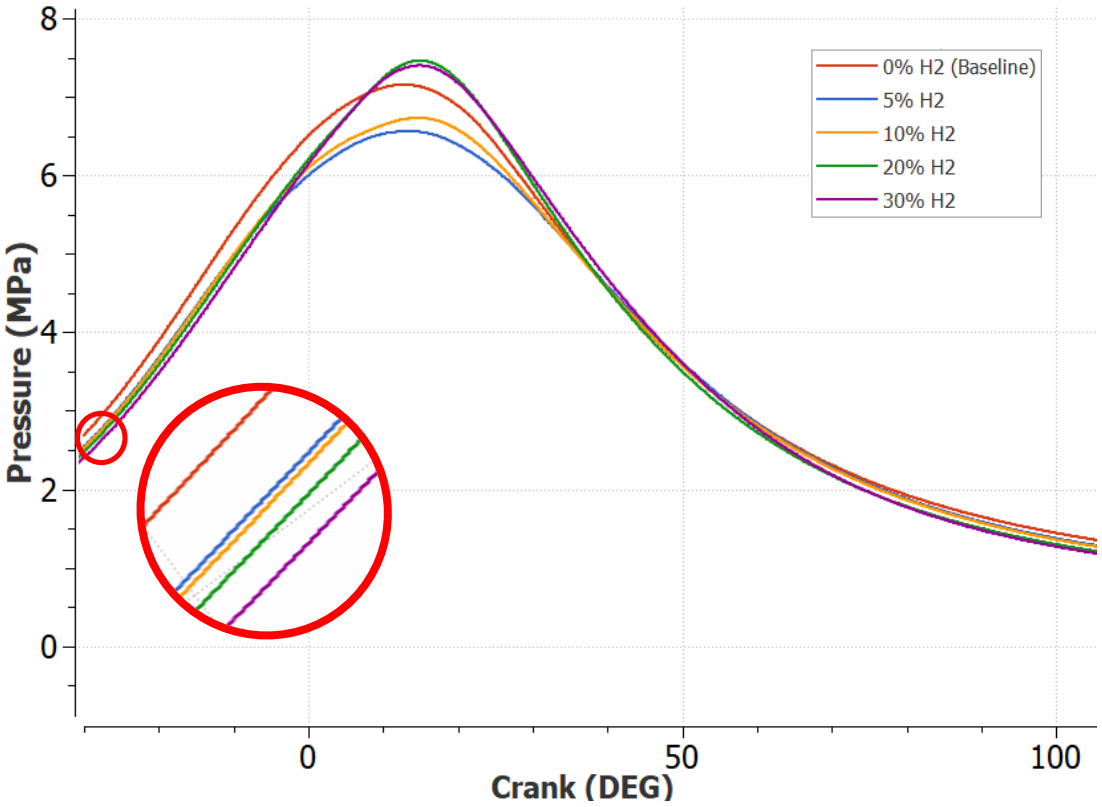

Figure 40. Pressure vs. crank angle for power-matched gas blends.

Figure 41 shows the amount of CH4 vs. crank angle for each gas mixture. This figure shows the lower amounts of CH4 as the hydrogen substitution increases. Table 5 contains the numerical amounts for the unburned CH4. The table also includes the percentage unburned for each gas mixture. Similar to the previous section, a percentage for the reduction of trapped CH4 compared to the baseline and an unburned percentage relative to the baseline are included. These give a better understanding that the reduction of CH4 emissions is not just due to substituting methane but also because the hydrogen burns more efficiently, thus leaving lower amounts of unburned CH4.

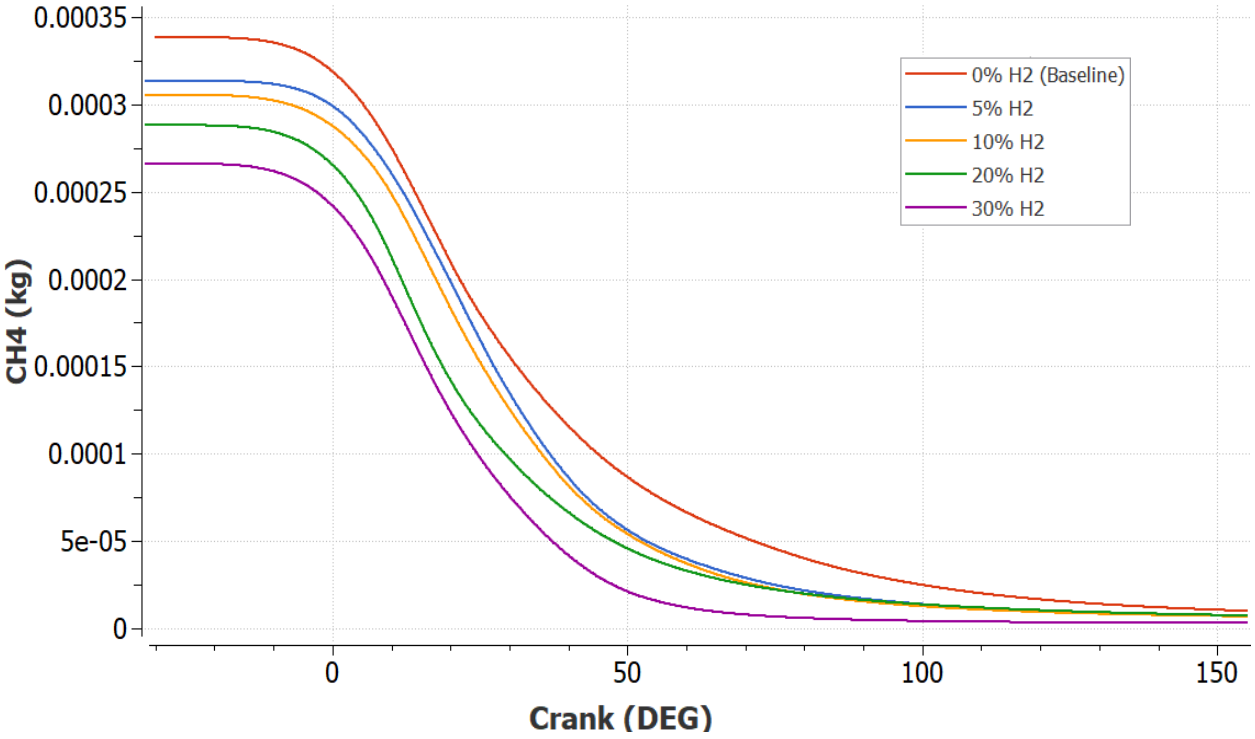

Figure 41. Trapped CH4 vs. crank angle for power-matched gas blends.

Table 5. Percentage of unburned CH4, reduction of trapped CH4, and Unburned percentage of CH4 relative to the baseline simulation.

	Trapped CH4 [g]	Unburned CH4 [g]	Percent Unburned	Trapped CH4 reduction from baseline	Unburned CH4 reduction from baseline
Baseline	0.338496	0.0101406	3.00%	**NA**	**NA**
5% H2	0.313638	0.00696535	2.22%	7%	31%
10% H2	0.305445	0.00700075	2.29%	10%	31%
20% H2	0.288129	0.00749492	2.60%	15%	26%
30% H2	0.266070	0.00319041	1.20%	21%	69%

Similar to the simulations that matched chemical energy to the baseline, the indicated power-matched simulations showed an increase in flame speed as the substitution of hydrogen increased. This is the most likely cause of the decreased unburned percentages. The faster flame speeds still allowed more fuel to be burned despite the adjustment to match indicated power.

Table 6. Flame speeds for each indicated power-matched gas mixture, based on conditions at spark.

	Pressure [MPa]	Temperature [K]	Equivalence ratio	Flame Speed [m/s]
Baseline	2.687	654.7	0.61	0.172
5% H2	2.536	654.8	0.61	0.180
10% H2	2.519	656.5	0.61	0.186
20% H2	2.438	656.6	0.61	0.200
30% H2	2.399	657.3	0.61	0.216

Figure 42 depicts the mass fractions of CH4 at the end of combustion for the baseline and the 30% hydrogen blend, similar to Figure 37. The significant differences that the hydrogen made in the combustion of natural gas are highlighted with red circles. These areas have lower mass fractions of CH4.

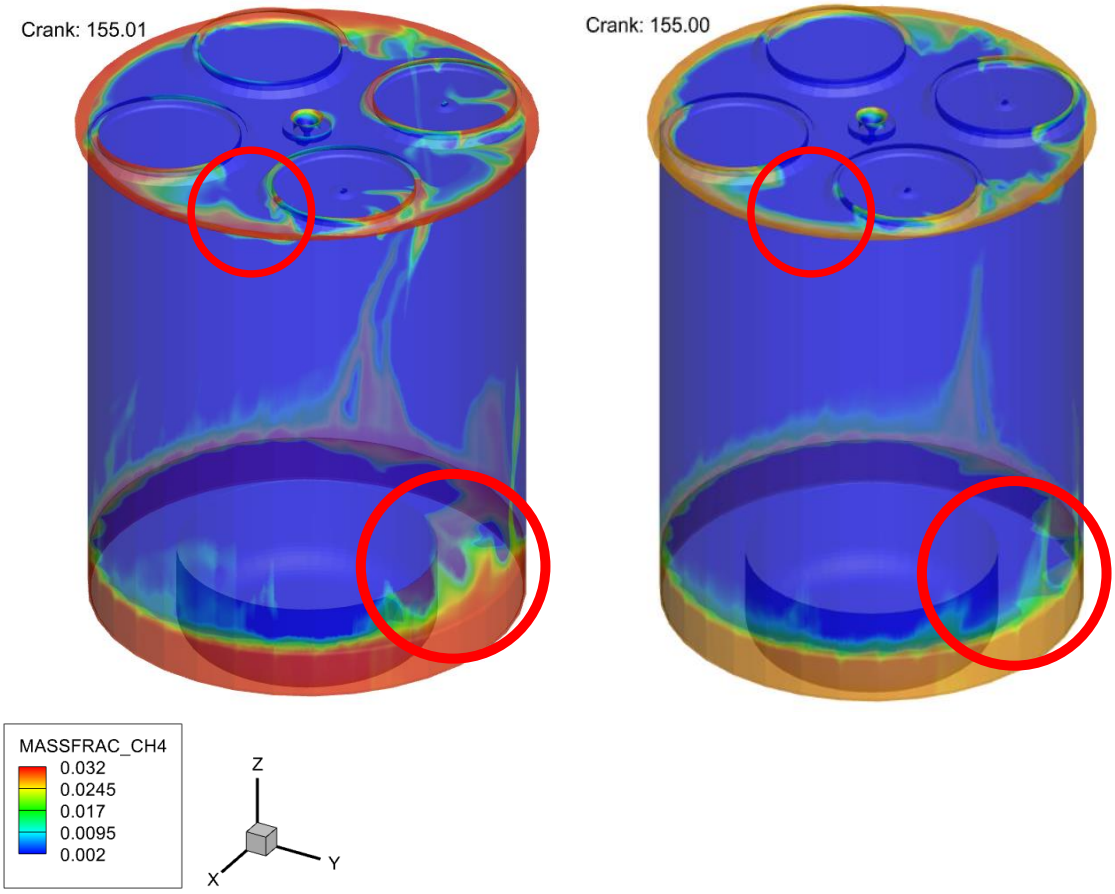

Figure 42. Mass fraction of CH4 at CA 155 for baseline simulation and 30% H2.

Figure 43 depicts the cross-sectional areas of some of the gas mixtures and compares the crevice volume to the baseline. This comparison is of the mass fraction of CH4. There are two different cross-sectional areas depicted. The red circles emphasize the areas that the preceding images are focused on.

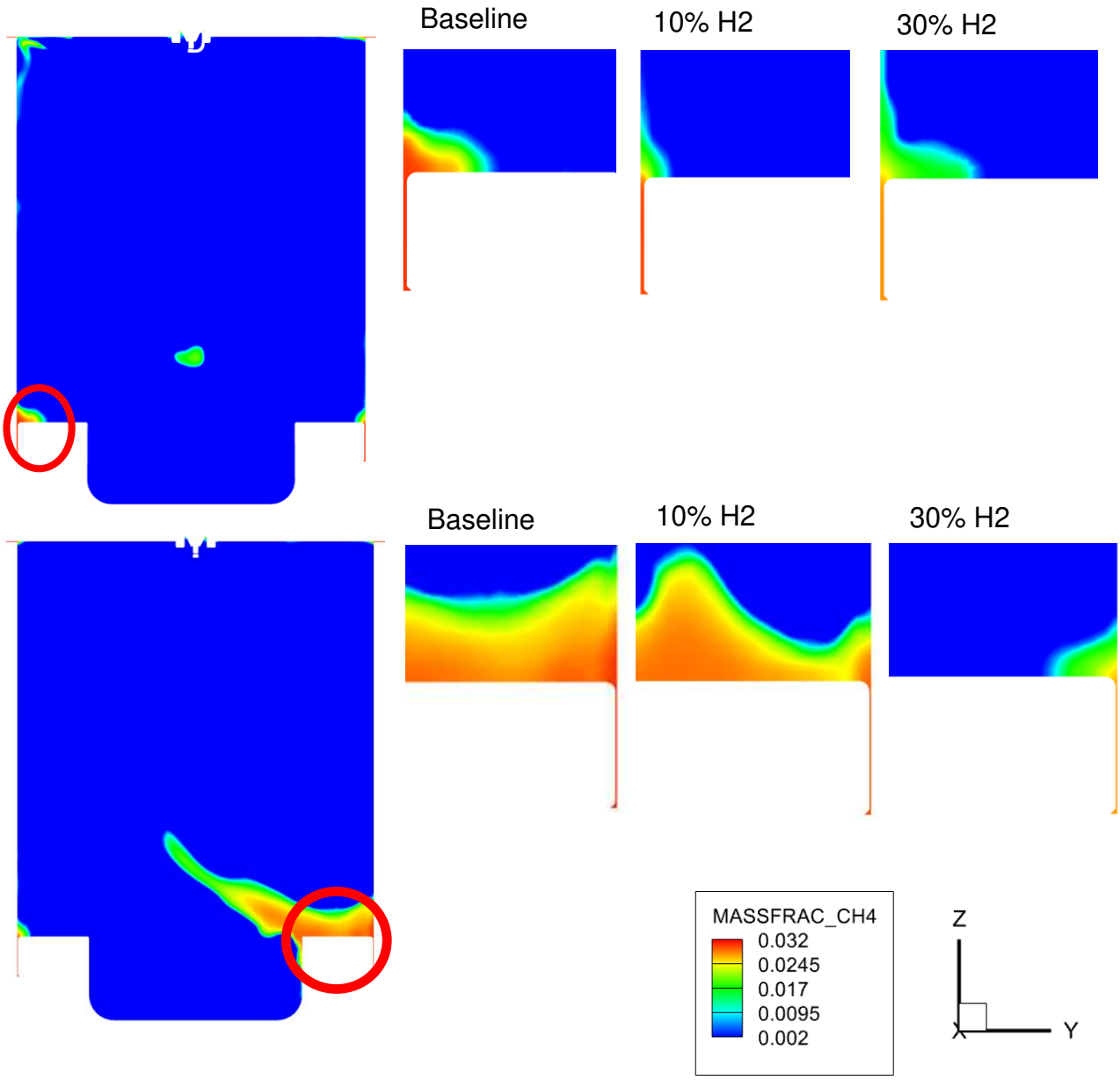

Figure 43. Cylinder cross sections depict CH4 mass fraction at various crank angles emphasizing the crevice volume for power-matched gas mixtures.

3.5 NOx Emission Results

The adiabatic flame temperature of hydrogen is higher than that of methane. Due to this, higher temperatures are expected when substituting hydrogen. Figure 42 depicts the average cylinder temperatures for the baseline and compares them to the 30% hydrogen blend. It can be seen that there are much higher temperatures associated with hydrogen-blended fuel. Even though these higher temperatures can aid combustion leading to less unburned fuel, they also create more NOx emissions. This is the case for the 30% hydrogen blend seen in Figure 44. Figure 45 depicts the NOx emissions produced in this case and the baseline to emphasize the increase.

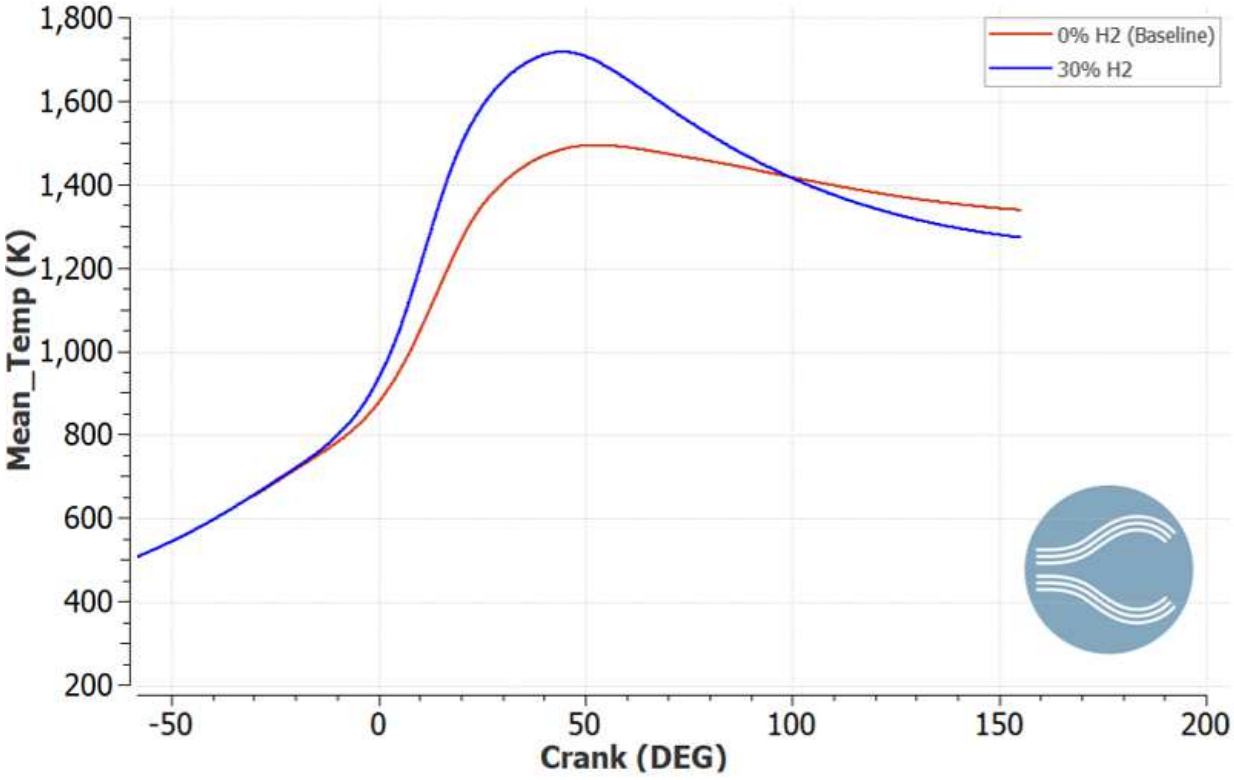

Figure 44. Mean cylinder temperature vs. crank angle for baseline simulation and 30% H2 blend.

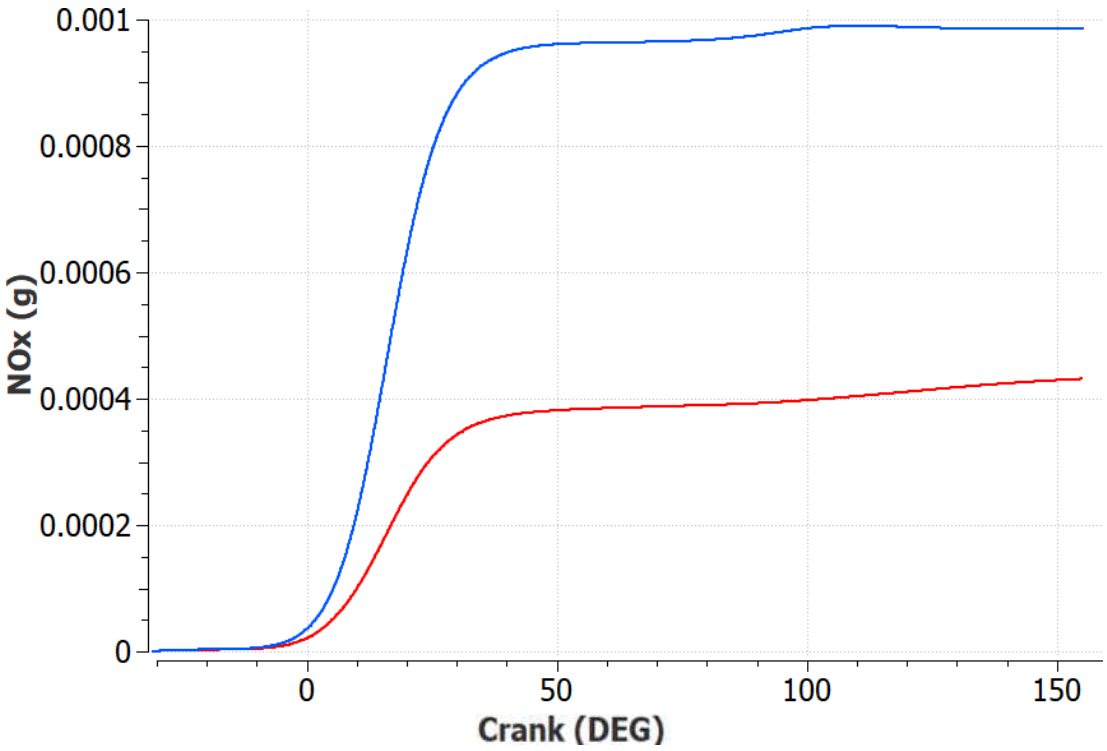

Figure 45. In-cylinder NOx vs. crank angle for baseline simulation and 30% H2 blend.

NOx emissions are restricted, so part of this research investigated mitigating the increased NOx emissions. The strategy being used is to lean the gas mixture further. This is done by adjusting the mass fraction input into the simulation to have more air and less fuel. More lean fuel mixtures have lower combustion temperatures, so this strategy is used to lower the combustion temperatures and thus lower the creation of NOx emissions. Figure 46 depicts the NOx levels for the different equivalence ratios and compares them against the baseline and the 30% H2-Blend. The ER of 0.5950 and 0.5900 is run initially. These simulations lower the NOx levels, but another simulation is run with an ER between these to maximize CH4 emission reduction while minimizing NOx emission creation. This final simulation has an ER of 0.5916. Table 7 contains the CH4 and NOx emissions values for the ER 0.5912, baseline, and 30% H2 power-matched blend.

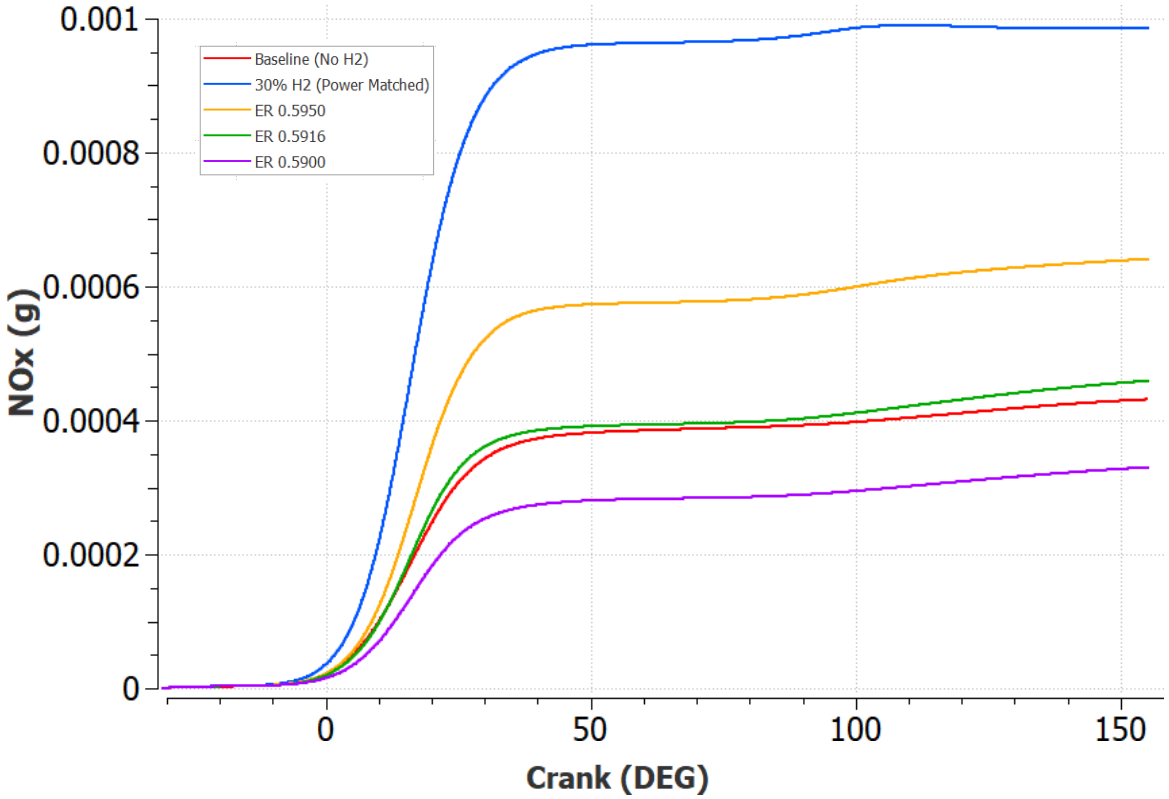

Figure 46. In-cylinder NOx vs. crank angle with various equivalence ratios compared to baseline simulation.

Table 7. NOx percentage, reduction of trapped CH4 percentage, and unburned CH4 percentage relative to the baseline for the 30% H2 blend with an ER of 0.5916.

	NOx [mg]	NOx Percentage relative to the baseline	Trapped CH4 [g]	Unburned CH4 [g]	Trapped CH4 reduction from baseline	Unburned CH4 reduction from baseline
Baseline	0.431492	NA	0.33850	0.010141	NA	NA
30% Power matched	0.989945	129.42%	0.26607	0.003190	21.40%	68.54%
ER 0.5916	0.459055	6.39%	0.25866	0.006907	23.58%	31.89%

Table 7 also shows that based on the simulation results, there is still a reduction of CH4 emissions greater than the substitution percent while mitigating the higher levels of NOx. Although this is the case, the amount that methane emissions are reduced is drastically lowered when leaning out of the mixture to reduce NOx. This decreases from 68% unburned CH4 relative to the baseline to 32%, which is only slightly higher than the H2 substitution of 30% by volume. However, after substituting H2, reducing the intake pressure to match indicated power, and leaning the gas mixture to meet NOx emissions of the baseline, the 30% H2 blend has a CH4 reduction approximately equal to 23.58% by mass. Thus, the percent methane reduction of 32% by mass is significantly greater than the reduction of trapped CH4 of 23.58%. Table 8 highlights the flame speeds for the baseline, the 30% hydrogen blend that is indicated power matched, and the adjusted equivalence ratio. Although adjusting the equivalence ratio lowers the flame speed of the 30% H2 blend, it is still faster than that of the baseline. It is for this reason that it is believed to be causing lower unburned CH4 amounts.

Table 8. Flame speeds for adjusted ER of the 30% indicated power-matched blends compared to the baseline.

	Pressure [MPa]	Temperature [K]	Equivalence ratio	Flame Speed [m/s]
Baseline	2.687	654.7	0.61	0.172
Power Matched 30% H2	2.399	657.3	0.61	0.216
Adjusted ER	2.404	658.5	0.5916	0.197

CHAPTER 4- ENGINE INSTALLATION

4.1 Engine Rebuild

In tandem with this research, a Caterpillar G3516J engine is to be installed at the Colorado State University Engines and Energy Conversion Laboratory. This engine started as a donation from Western Midstream and then was delivered to Wagner (a Caterpillar Dealer) in Aurora, Colorado. Figure 47 is the G3516J engine before moving to Wagner.

Figure 47. G3516J was donated by Western Midstream before the rebuild.

During its time at Western Midstream, the engine was operated through the projected lifetime and required a full overhaul upon arrival at Wagner. This process included a full disassembly of the bare engine block. This can be seen in Figure 48.

This step was critical to ensure that all seals, bearings, and other essential parts were up to Caterpillar specifications. Another example highlighting the importance of rebuilding the engine is the assessment of damage from the engine coolant. In the G3516J, coolant lines pass through the engine block and lead up to the head of the engine. Pitting can occur in the interface between the heads and the engine block, caused by the coolant traveling over time. These surfaces must be inspected for damage before being reassembled.

Figure 48. G3516J engine block after disassembly.

CSU collaborated with Caterpillar to confirm that all the new engine components arrived for the engine rebuild. For example, all seals, gaskets, and bearings were replaced. The crankshaft and the camshafts were inspected and approved to be reinstalled into the engine. Figure 49 shows the engine after the rebuild.

Figure 49. G3516J engine after rebuilding and before new paint.

4.2 Engine Removal

During the engine rebuild at Wagner, the CSU team was tasked with preparing for the new G3516J engine. The initial step was removing the Cummins QSK50 that was previously used as the test cell. This engine needed to be completely disconnected from the test skid, including unmounting the engine rails, in addition to disconnecting the coolant and pressure lines along with the sensory wires and driveshaft connections. Figures 50 and 51 depict what the QSK50 looked like before the disconnection.

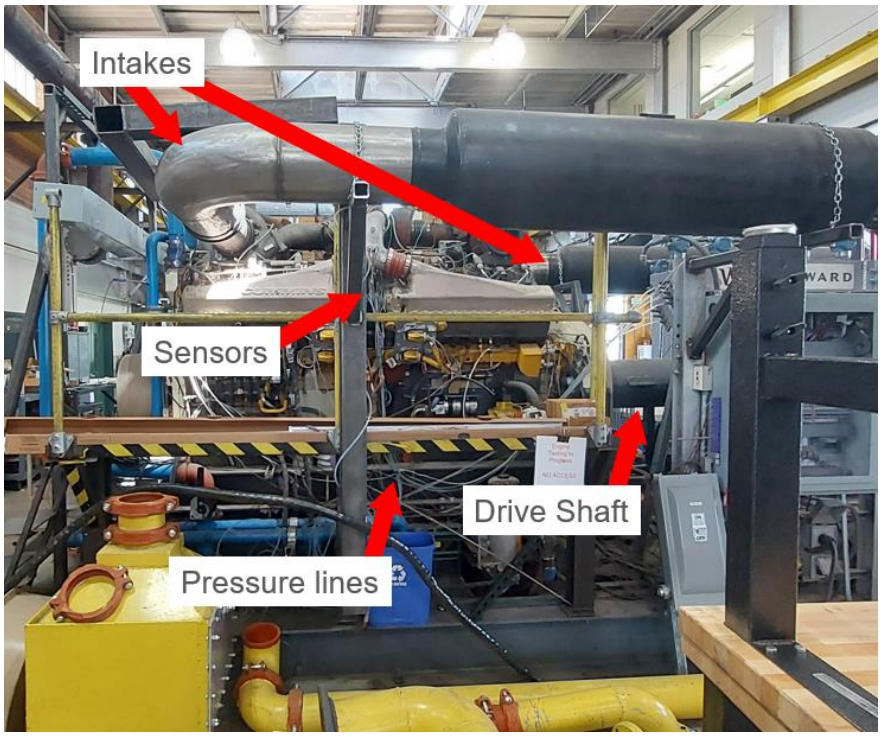

Figure 50. QSK50 Cummins depicting main components to disconnect-Side view.

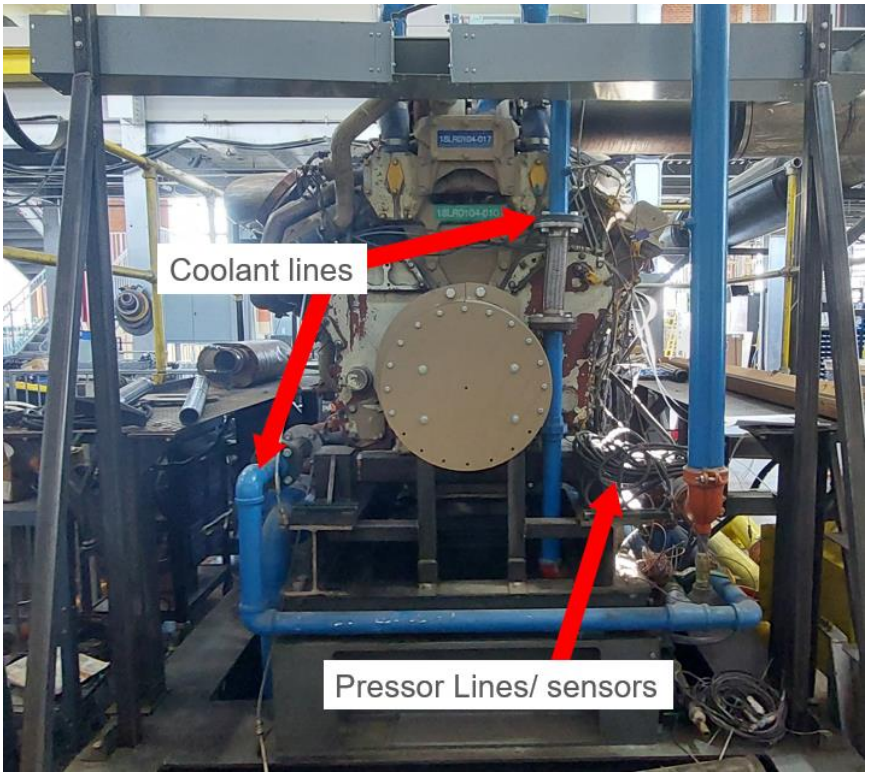

Figure 51. QSK50 Cummins depicting main components to disconnect-Front view.

Removal of the drive shaft was the first step in engine removal, beginning with the removal of the drive shaft cover. For safety reasons, a driveshaft cover was placed in the test skid, which needed to be unbolted and removed from the test skid to provide access to the bolts connecting the driveshaft to the engine and the dynamometer. Upon removing the bolts from the driveshaft, the in-house crane lifted the driveshaft into a storage area, where it awaited use on the new engine. The second step was removing the electrical connections, including each sensor that was the property of CSU, along with associated wiring from the engine. These sensors were stored together and organized with a listed inventory of all gathered parts. The pressure lines were removed with a similar process, as they were removed and stored with the sensors. Because the QSK50 is a diesel engine and the new Caterpillar engine is a natural gas engine, the diesel lines required removal. This included the hoses directly attached to the engine, piping that went into the basement of the testing facility, fuel filters, and flow meters. The flow meters and fuel lines were stored for possible future use, while the fuel filter was drained, dismantled, and recycled.

Taking place over a period of several weeks, the engine was eventually disconnected and ready to be lifted with the in-house crane. The engine was lifted off the test skid and placed on a roller system. A forklift was then used to push the engine out of the building to an open area. A larger crane hoisted the engine onto the back of a semi-trailer and the engine was shipped back to the manufacturer. Figure 52 shows the QSK50 being lifted, and Figure 53 shows the engine placed on the trailer.

Figure 52. Crane lifting QSK50 onto a semi-trailer.

Figure 53. QSK50 engine on semi-trailer just before transport back to Cummins.

With the QSK50 completely removed, the test skid was easily accessible. This allowed for the last step in preparing for the G3516J engine, cleaning the test cell. This included any remaining sensor wires, pressure lines, oil residue, and scaffolding left behind. Figure 54 shows the test skid before and after the thorough cleaning.

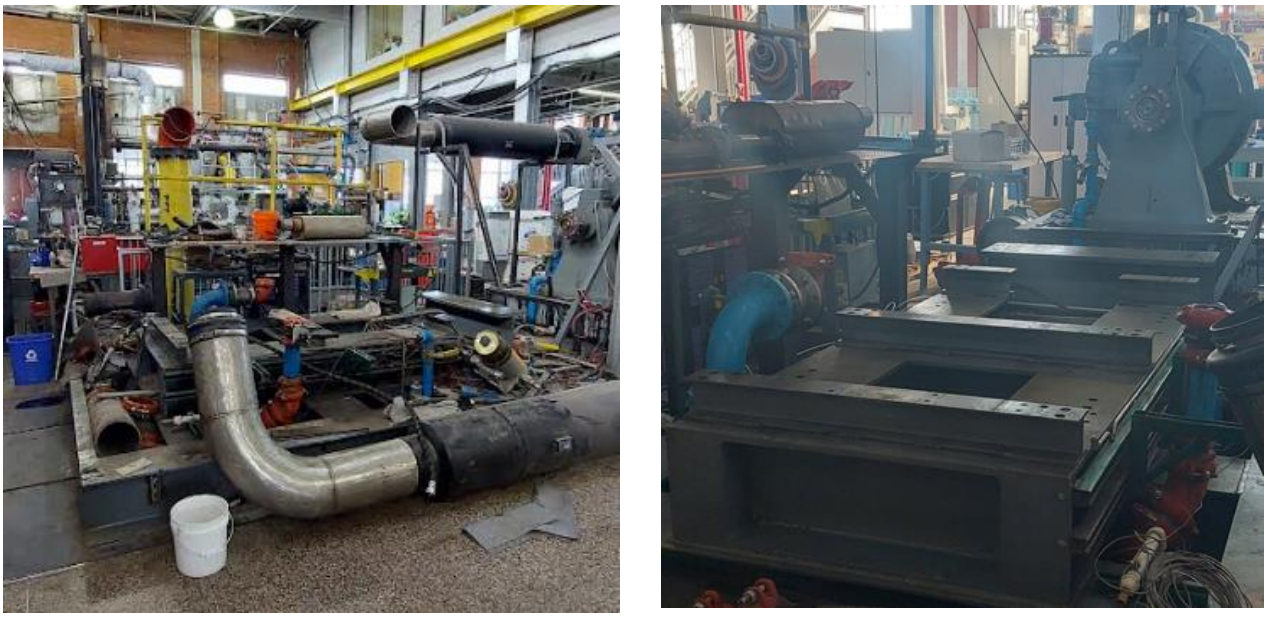

Figure 54. Before and after test cell preparation for G3516J engine.

4.3 Engine Installation

To outline this section of the engine installation process, Figure 55 demonstrates the main inputs and outputs, including the exhaust, fuel, jacket water-in, jacket water-out, and intercooler water-in and out, as well as the driveline connections.

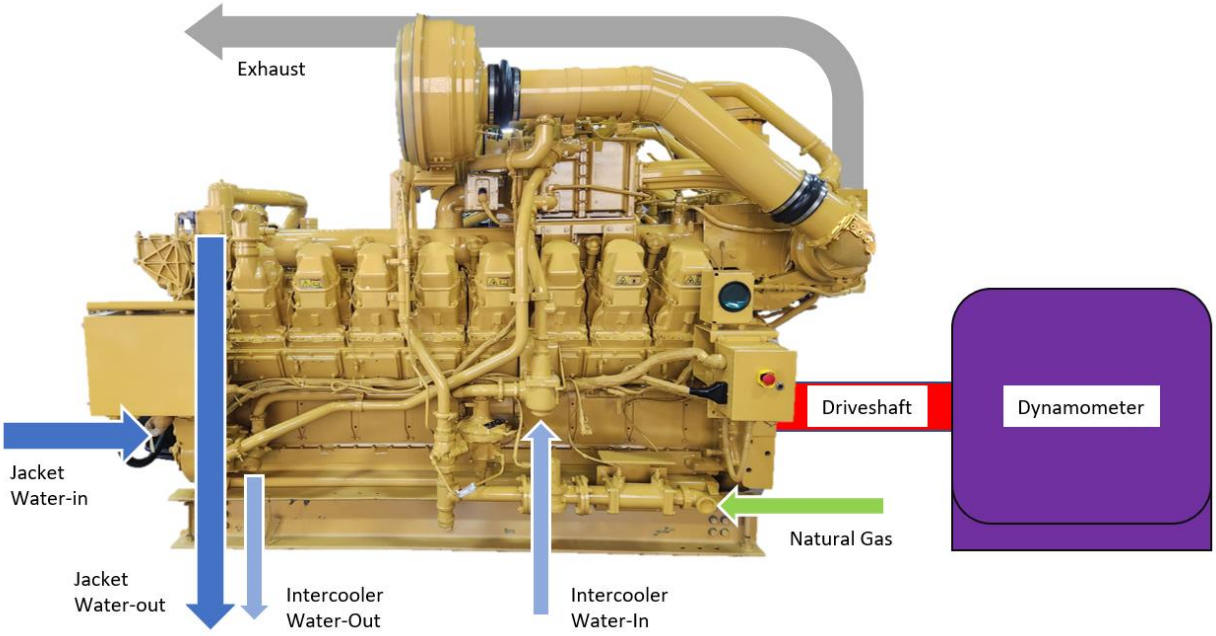

Figure 55. G3516J engine depicting main input and output connections to test cell.

Following the engine rebuild, including a new paint job, it was promptly shipped to the CSU Powerhouse Energy Campus on a semitrailer. Upon arrival, the engine was delivered to the back of the laboratory. The same crane used in the QSK50 removal was rented, arriving at the same time as the engine. The crane lifted the engine off the trailer and onto wood beams for easy forklift access later. Due to the snow and ice surrounding the laboratory at the time of delivery, the engine remained at the back of the building until a more appropriate opportunity, as minimal debris is required for the roller system to work properly. Figure 56 shows the engine being delivered to CSU and Figure 57 shows the crane lifting the engine off of the trailer.

Figure 56. G3516J engine arrival at the CSU Powerhouse facility.

Figure 57. Crane lifting G3516J engine off a semi-trailer and placed in the back of the laboratory.

Once the snow and ice melted, a forklift and the roller system pushed the engine into the laboratory, where it was lifted using the in-house crane and placed on the testing skid. The mounting rails on the G3516J contained holes that did not match the existing holes on the testing skid. The engine was also too low in comparison to the dynamometer, which if connected, would place the driveshaft at an unstable angle for the u-joints. To overcome this challenge, the mounting rails from a previous G3516J engine were integrated as a replacement. Figure 58 shows the rails that were removed and the new rails that were used. The engine then was sitting at the correct height, with all the mounting holes in alignment. Figure 59 shows the engine after the rails were replaced and sitting on the test skid with the mounting holes lined up.

Figure 58. Before and after the mounting rails on the G3516J engine were replaced.

Figure 59. G3516J engine on the test bed.

Measurements were taken for all of the mounting points, providing insight as to the number and thickness of shims that should be used. The mounting shims were required to ensure that the engine would be level overall, eliminating unnecessary engine wear. The first step in the leveling process was measuring the shim size for the outside four corners of the engine. This revealed that 1/8” shims were needed for the back two mounting points, while the front right corner needed a 0.005” shim. Once completed, measurements were taken for the remaining mounting points to determine the proper shim size for each. All of the shims were fabricated from shim stock using an industrial shear and a drill press. The proper shims were then placed at the appropriate

mounting locations. With these in place, bolts could then be dropped in the mounting holes, with the addition of leveling washers to level out the bolt heads to the mounting rail. The bolts were then fastened to the test skid and the engine was bolted down. Figure 60 shows the shims as well as one of the mounting points after the shims were installed.

Figure 60. Example of engine shim cut from shim stock, and one completed mounting point.

In addition to the mounting points, it is also critical to address the necessary driveline. The G3516J engine has a flywheel that requires a connection to the drive shaft. To connect these two parts, an adapter plate was designed and implemented. The initial step was to design the adaptor plate in solid modeling software. The plate needed to match the outside diameter of the flywheel as well as the hole pattern. Dimensions were pulled from drawings of the flywheel and confirmed with direct measurements. Holes needed to be created to match those located on the flywheel and driveshaft. The driveshaft holes require threads, as the engine lacks space for a

fastener to be placed on the backside of the plate, and the bolts must be fastened to the plate itself. Figure 61 shows the engineering drawing of the adaptor plate.

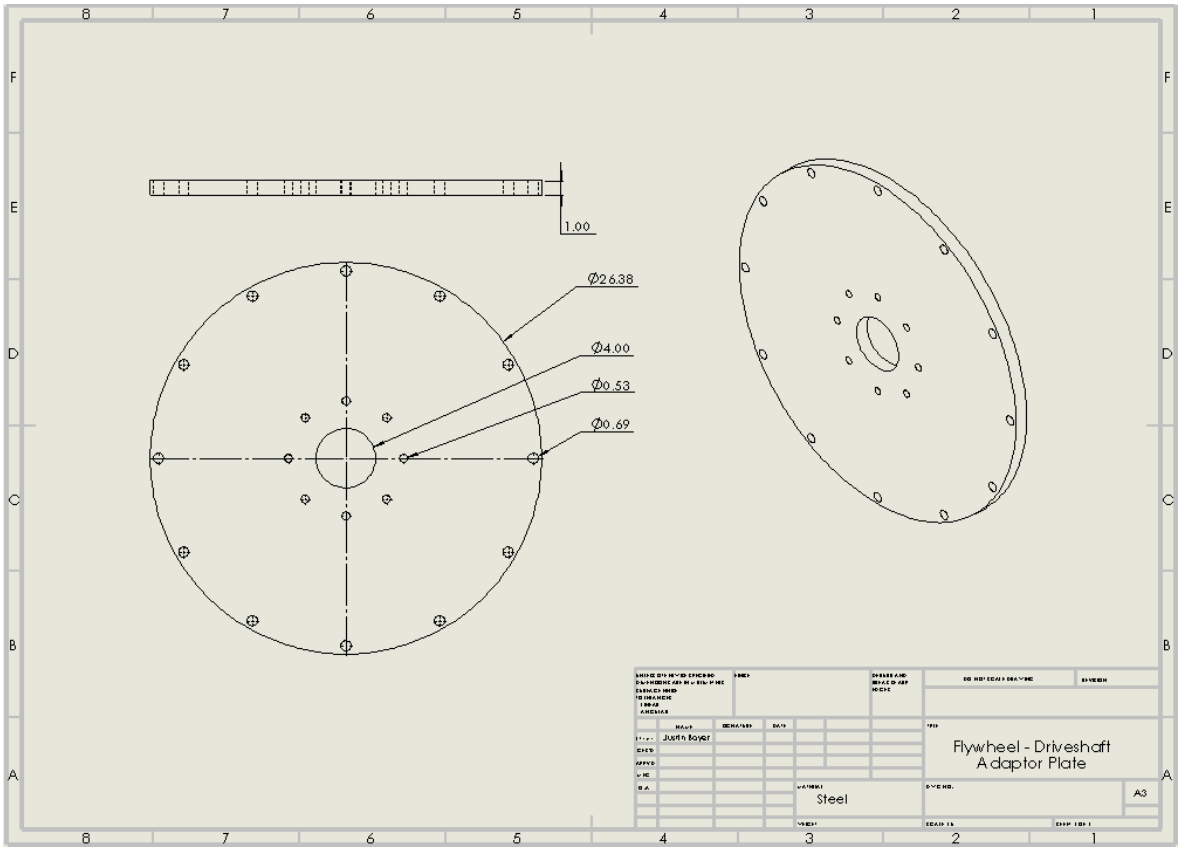

Figure 61. Detailed drawing of flywheel/ driveshaft adaptor plate.

As displayed in the figure, the outer ring of holes is for the flywheel of the engine, while the inner ring is for the driveshaft. The CSU engineering team and Rapid Prototyping Lab decided on the material and thickness of the plate upon completion of the plate design. The specifications were sent to the Rapid Prototyping Lab to be cut utilizing the in-house water jet. The RPL then tapped the holes and delivered the plate to the G3516J engine. The next step involved using the in-house crane to lift the plate to the flywheel, where it was bolted to the engine. Once secured, the drive shaft was maneuvered via the crane, moving it closer to the adaptor plate where it was bolted to

the adaptor and the dynamometer. The final step was to design a cover for the flywheel, allowing for the safety and well-being of all individuals operating the engine. This design process was similar to the flywheel adaptor plate, as the parts were designed in 3D modeling software and then given to the RPL lab to cut via the water jet. When complete, the finalized parts were installed on the engine. Figure 62 shows the design for the flywheel cover.

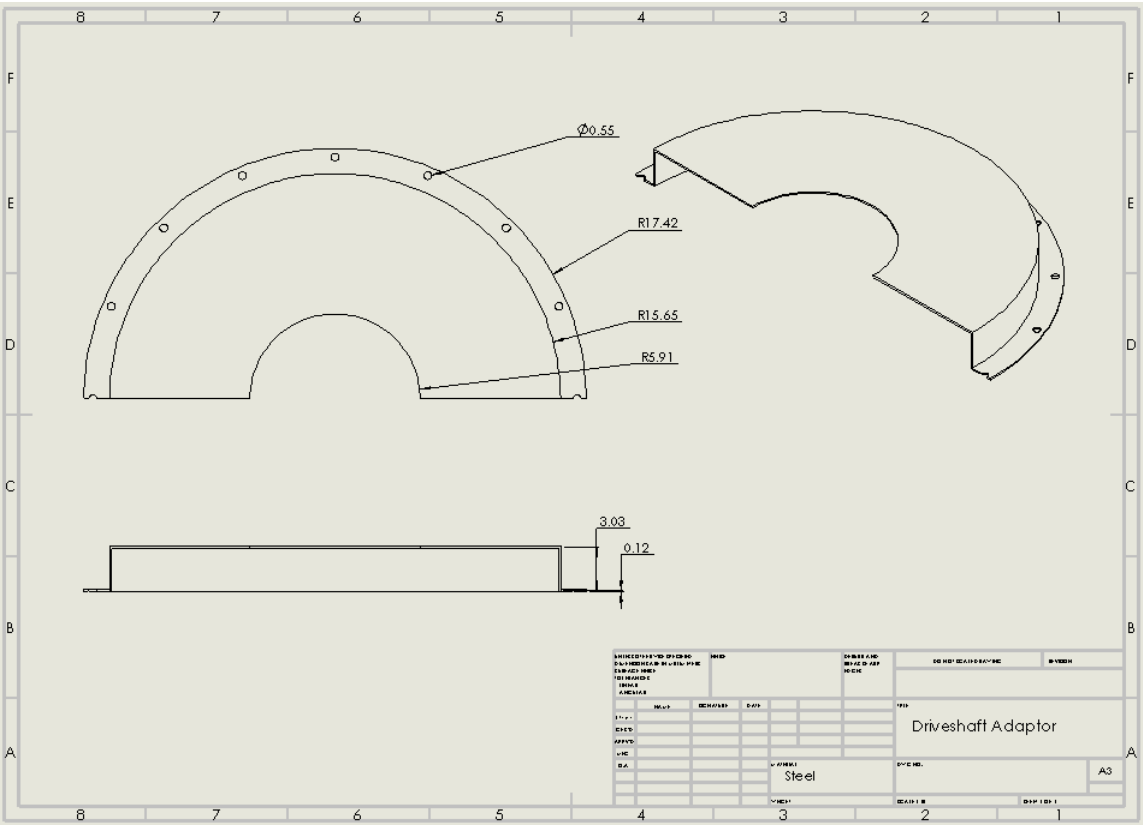

Figure 62. Flywheel cover design.

As the engine installation progressed, the next project was the coolant lines. The engine has both intercooler lines and jacket water lines with water flowing in and out. At the laboratory, most established engines obtain water from a common coolant tower located in the basement.

The QSK50 utilized lines coming from this coolant tower, originally modified for the G3516J. The jacket water-in required a 180-degree rotation to adequately fit the Caterpillar engine. Once flipped via the crane, the previously used butterfly valve was replaced with a new flanged valve, ensuring an elevated level of safety. The jacket water line then had a bellow and flange adaptor attached. The flange adaptor transitions to a 4-inch pipe, which features a grooved surface. Gruvlok clamps were used to clamp the appropriate lengths of pipe and elbows to reach the desired jacket water-in port on the engine. Although the elbows were grooved by the manufacturer, the piping still needed to be grooved by hand. This was done using an in-house groover after the pipes were cut to the correct length using a horizontal band saw. To attach properly, the port required the fabrication of an adaptor. Figure 63 shows a drawing of the part that was sent to the RPL lab to fabricate. When received, it was successfully installed on the system.

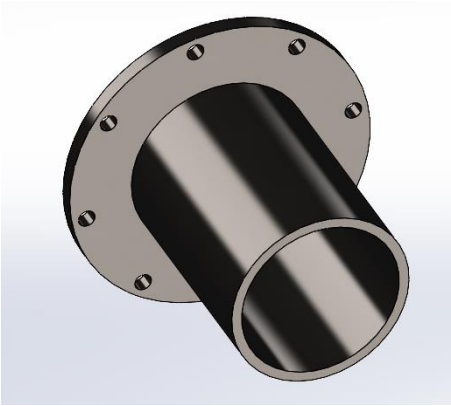

Figure 63. Jacket water-in adaptor

When installing the jacket water-in, integration of a hose to connect the port adaptor to the 4-inch piping became necessary. This hose needed to have the correct size, temperature, pressure, and chemical/oil resistance. This is because trace amounts of oil are located in the coolant tower. Moreover, the hose was clamped to the system

and the jacket water-in lines were complete. A similar process was replicated for the jacket water-out lines. A specialized hose connected the engine to the piping. In this system, the hose also needed to act as a reducer, allowing the engine's port with a 5.5-inch diameter to be reduced to a 4-inch pipe. The pipe lengths and elbows were then added to the system employing the same groove method. Within the longest section of piping, a portion was removed to place a grooved ball valve. Finally, the jacket water-out was secured through the creation of a bracket system mounted to the test skid. The jacket water-out system can be seen in Figure 64. For the intercooler piping, the process proved to be very similar, except with the implementation of a 2-inch pipe. This 2-inch pipe was threaded instead of grooved.

Figure 64. Jacket water-out line highlighting the ball valve for manual shut-off.

Prior to the QSK50, a natural gas engine was installed. Several natural gas lines remained from this equipment; however, there was still extensive work to complete. From the previous lines, a flanged connection was implemented and routed around unmovable, existing water lines. For the former engine, the natural gas line sat at 3 inches, and a reducer was required to decrease the line to 2 inches. In this case, the 2-inch pipe was routed through the remainder of the basement, then ran upwards through the floor of the test skid. Channel hangers provided additional pipe support where needed. After emerging from the floor, an emergency shutoff is provided via the addition of a pneumatic valve. This valve was placed as close to the engine as possible, as in the event of a shut-off, minimal amounts of natural gas could still advance to the engine. Figure 65 shows the natural gas lines in the basement and Figure 66 shows the lines that were above the test skid floor.

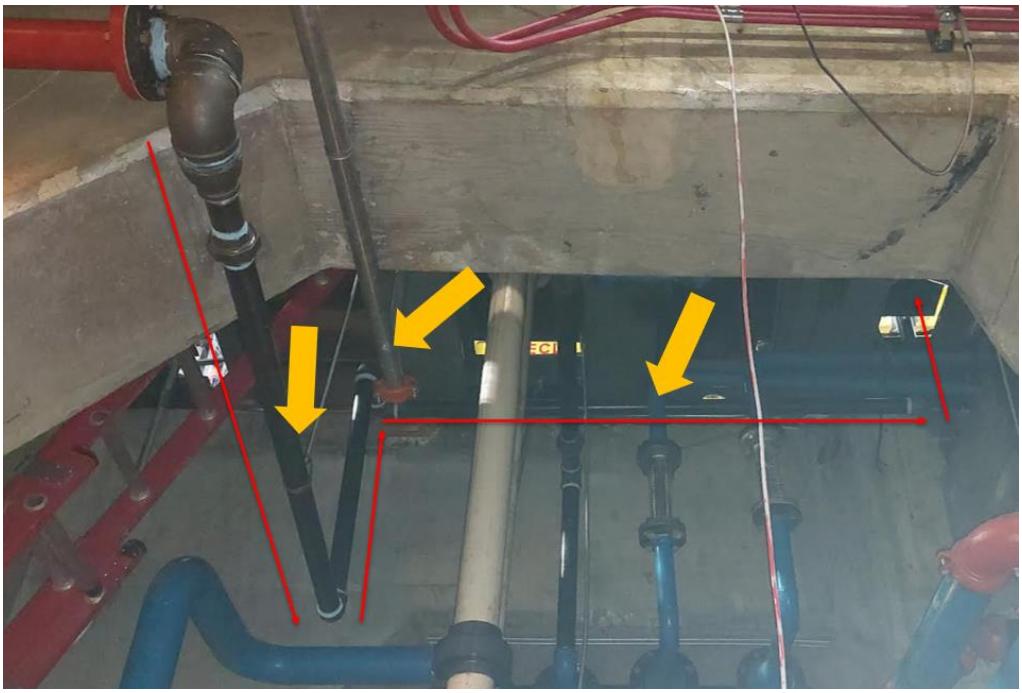

Figure 65. The natural gas line ran underneath the G3516J engine. The red arrows depict the flow of the natural gas line, and the yellow arrows point out the mounting points to secure the pipes.

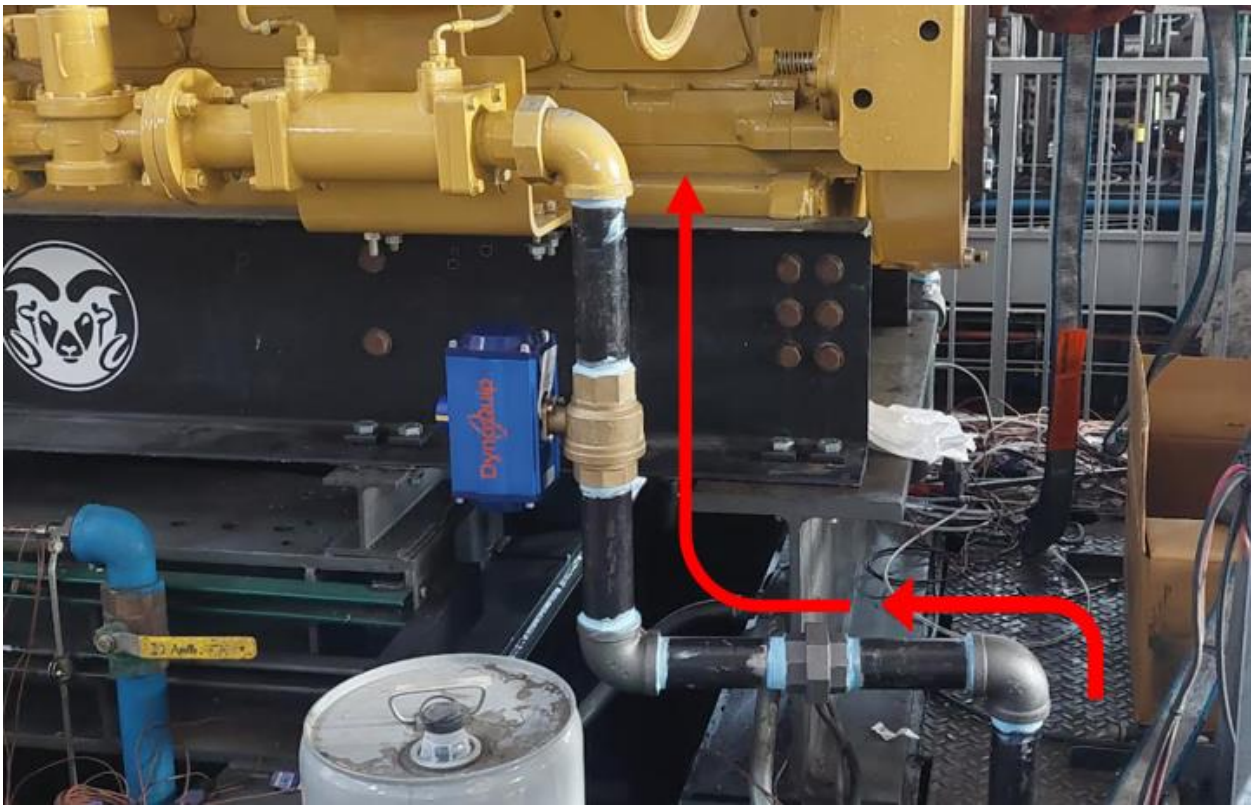

Figure 66. The natural gas line ran above the floor of the G3516J engine. The red arrows depict the flow of natural gas.

With an ongoing collaboration, CSU and Caterpillar worked together to order and integrate an exhaust bellow and adaptor. The below absorbs engine vibrations that would otherwise damage the exhaust system, which is essential because the exhaust used in the facility is mounted directly to the building. The G3516J features an exhaust port with a diameter of 10.67 inches, and an adaptor was used to elevate the diameter to 12 inches. This increase ultimately lowers the cost of exhaust piping due to the accessibility of a 12-inch pipe, as the 10.67-inch diameter would require customized piping. To uphold the extensive weight of the exhaust, the previously used QSK50 supports were modified and placed on the test skid.

CHAPTER 5- CONCLUSIONS

This research was conducted to test multiple methods for lowering CH4 emissions in a Caterpillar G3516J engine model using Converge Computational Fluid Dynamics. The first step in this research was to create an accurate baseline model for one cylinder of the G3516J engine. Once the baseline was tuned, the first unburned CH4 reduction method utilized controlled end gas auto-ignition. This was investigated by advancing the model spark timing. Although there were no apparent signs of EGAI either in the 3D renderings of the simulations or in the pressure curves, advancing the spark timing did prove to lower the unburned CH4. The second method researched was hydrogen substitution by volume, where the equivalence ratio and the chemical energy of the trapped mass of fuel were matched. These results yielded significant decreases in unburned CH4 amounts across all gas mixtures (5% H2, 10% H2, 20% H2, and 30%H2). The CH4 emissions were decreased from the baseline amount but the indicated power from these simulations was higher than the baseline. The next step in this research was to lower the intake manifold pressure further to match the indicated power to the baseline value. Even after doing this, the hydrogen and natural gas blends decreased unburned CH4. Because more fuel is burned and hydrogen burns much hotter than natural gas, higher temperatures cause significant increases in NOx emissions. The 30% H2 blend was assessed for a NOx emission strategy. The strategy was to lower the equivalence ratio further to reduce the in-cylinder temperatures and thus lower the NOx emissions. This proved to lower the NOx emissions as well as unburned methane emissions. The results from these simulations are listed below.

Finally, this research explored the steps taken to install a G3516J engine at the Engine and Energy Conversion Laboratory at CSU.

End gas Auto-ignition unburned CH4 percentages compared to the baseline.

- EGAI could not be induced with the current engine operating conditions.
- Advancing spark timing did prove to lower unburned CH4 from 3.00% to 2.26%.

Hydrogen substitution results in unburned CH4 emissions for chemical energy-matched gas mixtures.

- Blending Hydrogen lowered the unburned percentage of methane by 67. 08% compared to the baseline in the most extreme case, where there was only a reduction of 11.56% due to the substitution. This was the case for 30% H2 Blend
- The 5% H2 Blend has the lowest substitution percentage drop for CH4 at 1.23% but saw a reduction of unburned CH4 of 44.55% compared to the baseline.

Hydrogen substitution results for unburned CH4 emissions for indicated power-matched gas mixtures.

- After Lowing the trapped mass to match the indicated power of the baseline, it was observed that the unburned CH4 Percentage dropped from 3.00% to 1.20% for the 30% H2 Blend
- The 30% H2 Blend had an unburned percentage drop of 69% compared to the baseline with only a 21% fuel substitution drop .

NOx emissions reduction compared to baseline for 30% H2 Blend.

- The 30% H2 substitution had a 129% increase in NOx emissions compared to the baseline but was reduced to 6.39% through leaning of the fuel and air.
- The leaner gas mixture still has a 31.89% unburned CH4 reduction with a 23.58% reduction due to the gas substitution while relatively maintaining NOx emissions.

The results from the NOx mitigation strategy proved to lower both the CH4 emissions and the NOx emissions. This came at the cost of lower indicated power. Future work will consist of investigating strategies to adjust for this power loss. Future work for this research will also include finalizing the G3516J installation. After this is complete, preliminary testing can begin, to help validate the CFD models. This includes timing sweeps and fuel blend experiments on the G3516J. In the future, this research will also include engine geometry changes. For example, raising the top-land Crevice volume could prove to lower CH4 emissions by creating smaller volumes for the CH4 to avoid combustion. Finally, this research will look into other fuel types that could be used to lower CH4 emissions similar to hydrogen.

REFERENCES

[1] U.S. Energy Information Administration - EIA - independent statistics and analysis. Use of natural gas - U.S. Energy Information Administration (EIA). (n.d.). Retrieved January 17, 2023, from https://www.eia.gov/energyexplained/natural-gas/use-of-natural-gas.php#:~:text=The%20United%20States%20used%20about,of%20U.S.%20total%20energy%20consumption.

[2] Environmental Protection Agency. (n.d.). Overview of Greenhouse Gases. EPA. Retrieved April 18, 2023, from https://www.epa.gov/ghgemissions/overview-greenhouse-gases

[3] Vaughn, T., Luck, B., Williams, L., Marchese, A., & Zimmerle, D. (2021, January 9). Methane Exhaust Measurements at Gathering Compressor Stations in the United States. ASC Publications. Retrieved April 18, 2023, from https://pubs.acs.org/doi/10.1021/acs.est.0c05492

[4] Department of Energy announces $22.5 million to reduce carbon emissions from manufacturing. Energy.gov. (n.d.). Retrieved April 18, 2023, from https://www.energy.gov/eere/amo/articles/department-energy-announces-225-million-reduce-carbon-emissions-manufacturing

[5] Turns, S. R., & Haworth, D. C. (2021). *An introduction to combustion: Concepts and applications*. New York: McGraw-Hill.

[6] Konig, G., & Sheppard, C. (1990). End gas autoignition and knock in a spark ignition engine - JSTOR. Retrieved April 23, 2023, from https://www.jstor.org/stable/44580422

[7] Gholami, R., Alyani, M., & Smith, K. (2015). Deactivation of Pd Catalysts by Water during Low Temperature Methane Oxidation Relevant to Natural Gas Vehicle Converters. *Catalysts, 5*(2), 561-594. doi:10.3390/catal5020561

[8] Kinnunen, N. M., Nissinen, V. H., Hirvi, J. T., Kallinen, K., Maunula, T., Keenan, M., & Suvanto, M. (2019). Decomposition of Al2O3-Supported PdSO4 and Al2(SO4)3 in the Regeneration of Methane Combustion Catalyst: A Model Catalyst Study. *Catalysts, 9*(5), 427. doi:10.3390/catal9050427

[9] Salomons, S., Hayes, R., Poirier, M., & Sapoundjiev, H. (2003). Flow reversal reactor for the catalytic combustion of lean methane mixtures. *Catalysis Today, 83*(1-4), 59-69. doi:10.1016/s0920-5861(03)00216-5

[10] Nadaleti, W. C., & Przybyla, G. (2018). Emissions and performance of a spark-ignition gas engine generator operating with hydrogen-rich syngas, methane and biogas blends for application in southern Brazilian rice industries. *Energy, 154*, 38-51. doi:10.1016/j.energy.2018.04.046

[11] Wallner, T., Ng, H., & Peters, R. (n.d.). The effects of blending hydrogen with methane on engine operation ... Retrieved April 18, 2023, from

https://www.researchgate.net/profile/Robert-Peters-13/publication/238058797_The_Effects_of_Blending_Hydrogen_with_Methane_on_Engine_Operation_Efficiency_and_Emissions/links/551a8a690cf26cbb81a2eccb/The-Effects-of-Blending-Hydrogen-with-Methane-on-Engine-Operation-Efficiency-and-Emissions.pdf

[12] Heywood, J. B. (1988). *Internal Combustion Engine Fundamentals*. Singapore: McGraw Hill International Editions.

[13] Bayliff, S., Windom, B., Marchese, A., Hampson, G., Carlson, J., Chiera, D., & Olsen, D. (2020). Controlled End Gas Auto Ignition With Exhaust Gas Recirculation on a Stoichiometric, Spark Ignited, Natural Gas Engine. *ASME 2020 Internal Combustion Engine Division Fall Technical Conference*. doi:10.1115/icef2020-2979

[14] Soylu, S. (2003). Development of an autoignition submodel for natural gas engines⋆. *Fuel, 82*(14), 1699-1707. doi:10.1016/s0016-2361(03)00147-9

[15] Converge CFD Software. Convergent Science Press. (n.d.). https://convergecfd.com/

[16] Smith, G.P. (n.d.) et. Al. *WHAT'S NEW IN GRI-Mech 3.0*. GRI-Mech 3.0. Retrieved April 29, 2022, from http://combustion.berkeley.edu/gri-mech/version30/text30.html

[17] Jolla, L. (2012). *The San Diego Mechanism*. Chemical Mechanism: Combustion Research Group at UC San Diego. Retrieved April 29, 2022, from https://web.eng.ucsd.edu/mae/groups/combustion/mechanism.html

[18] Marchese, A. (2020). *Chemical Kinetic Mechanisms*. Anthony Marchese's Home Page. Retrieved April 29, 2022, from https://www.engr.colostate.edu/~marchese/research.html